Alloying propagation in nanometric Ni/Al multilayers: A molecular dynamics study

V. Turlo, O. Politano, Florence Baras

Alloying propagation in nanometric Ni/Al multilayers: A molecular dynamics study.

V. Turlo, O. Politano and F. Baras*

Laboratoire Interdisciplinaire Carnot de Bourgogne,

UMR 6303 CNRS-Université Bourgogne Franche-Comté,

9 Avenue A. Savary, BP 47 870, F-21078 DIJON Cedex, FRANCE

In nanometric metallic multilayers such as Ni/Al, the alloying reaction proceeds in the form of a propagating wave. We studied the different phase transformations involved in the reactive wave propagation by means of molecular dynamics. The focus was on a specific regime that involves melting of reactants, intermixing of reactants and formation of an intermetallic compound. We found that the wave consists in two stages. The first front is associated with a dissolution process and propagates at several meters per second while the second front is due to the crystallization of the final product and is slower leading to a specific microstructure with alternated large grains of NiAl and liquid regions in the front propagation direction. Three main exothermic processes were identified, including grain coarsening. Their respective contributions were evaluated. We developed a new texture analysis tool that allowed us to follow the evolution of the microstructure and the dynamics of the grain orientation.

I. INTRODUCTION

Nanometric metallic multilayers (N2M) - also named reactive multilayer thin films or nano-foils - are made up of alternated layers of metals A and B, whose thickness is nanometric (typically 4-100 nm) [1–3]. A N2M's sample contains hundreds, or even more, of superposed thin metallic films: A-B-A-... (e.g. Ni-Al, Ti-Al, Pt-Al). The reaction in an N2M can be initiated by a local heating at one edge of the sample, by means of spark or laser. Once ignited, the reaction propagates in a self-sustained way without any further supply of energy. The ignition can take place even for very low initial temperature (300-400 K) and the reaction propagates at high velocities up to several dozens of meters per second [5]. N2Ms generate a multitude of practical applications in reactive joining technologies [4] and as energetic materials. The control of the technology requires a deep understanding of the phase transformations associated with the self-propagating high-temperature

*Electronic address: florence.baras@u-bourgogne.fr

synthesis (SHS) of the reactants A and B into the final products AB (intermetallic compound).

SHS in N2Ms is an active field because many features remain puzzling. For instance, it was proven experimentally that the combustion wave consists of two stages [6]. But the explanations diverge [7, 8]. More generally, the challenge is to relate the microstructure to the characteristics of the propagation wave, including the transient states. In this respect, Molecular Dynamics (MD) offer a good approach in understanding the development of basic mechanisms that occur in nanofoils during the reactive propagation. Concerning the nanolayered Ni-Al system, MD has been used to study some specific aspects: the possibility of a reaction at a relatively low temperature and the development of intermetallic phases [9], the effects of the as-deposited microstructure on the initiation of the Ni-Al reactive multilayer [10], the interdiffusion of Ni and Al at interfaces [11, 12], the role of pressure on the initiation of the reaction [13], the nucleation and growth of the B2-NiAl phase at interfaces [14] and shock-induced alloying reactions in Ni/Al nanolaminates [15]. Note that Ni-Al refers to all films containing layers of Ni and Al regardless of their quantitative ration; Ni/Al signifies that the ratio between Ni and Al in two adjacent layers corresponds to the equimolar average composition of the film. Recently, molecular dynamics were used to simulate large systems of about 1 μm. High-temperature, self-propagating reactions were investigated in nanolayered Ni-Al foil [16], and reaction mechanisms were studied in thermally ignited core/shell Ni/Al wires [17]. Isothermal simulations were developed to explain the main features of the microstructures observed in quenched Ni-Al systems [18].

The aim of our work was to study a propagation regime which combines different processes: melting, mixing and crystallization. It was proven that the dissolution and intermixing is a key step in the propagation mechanism [19]. But the development of crystallization during the SHS process is not completely understood. Rogachev has suggested in [20] a mechanism for the rapid crystallization of melts in reactive multilayers nanofilms, following the scheme drawn in Fig. 1. Let us assume that two reactants A and B have a distinct melting temperature, $T_m^{\mathrm{B}} < T_m^{\mathrm{A}}$, as is the case in the Ni-Al system. The first front to propagate is the front of the melting of reactant B. Reactant A progressively dissolves in the molten zone as a function of the local temperature. This leads to a zigzagged profile of solid A into a A+B liquid solution, as shown in the scheme. While the dissolution proceeds, an exothermic mixing takes place. The next slice only contains a liquid solution at high temperature with a stoichiometry that depends on the composition of the system. This molten slice can be in a liquid metastable state, for the compound AB, if $T_m^{\mathrm{B}} < T_m^{\mathrm{A}} < T_m^{\mathrm{AB}}$. In this case, the product AB crystallizes from the undercooled melt. The first front of the melting of B is followed by the front of the melting of A and by the front of the crystallization of the

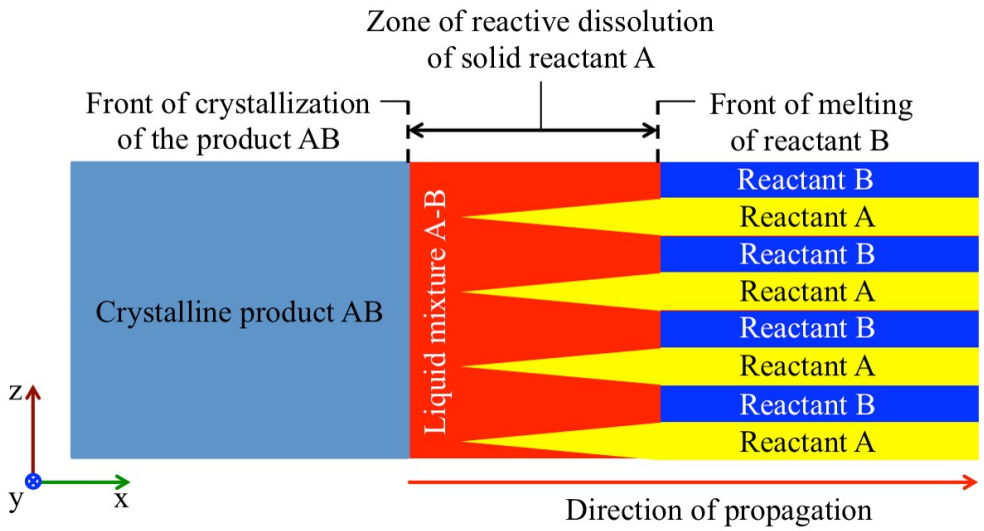

FIG. 1: Scheme of a model for rapid crystallization in multilayer nanofilms (from [20]).

product. Here, two heat sources act as energy supply: exothermic mixing and crystallization of the undercooled melt.

In order to study the crystallization of melts in Ni/Al N2Ms, specific MD simulations were performed. Three representative systems were prepared: a small system, a long system and a thick system. The same initial condition was imposed: an equiatomic stoichiometry with an initial temperature of 300 K. In the long sample the length was much greater than the width of the conduction zone. This allowed accurate estimation of the main characteristics of the reactive front. The effect of the elongated shape on the final microstructure was also investigated. The geometry of the thick sample results in a large number of $B2$-NiAl grains. The orientation of $B2$ grains in the thick system was analyzed to determine the texture of the final product. The small sample was used to study the effect of an initial annealing on the kinetic characteristics of the reactive front. The conditions for grain formation from melts were also discussed.

II. SIMULATION DETAILS

The molecular dynamics (MD) simulations were performed with the LAMMPS MD software [21] and EAM Ni-Al potential, developed by Mishin et al. [22]. This many-body force field is based on accurate potentials for pure Ni and Al. It was also developped to precisely describe physical properties (e.g., melting temperatures) and the relative stability of intermetallic phases across the Ni-Al phase diagram. It is widely used to study systems such as reactive Ni-Al nanometric

multilayers where phase transformations occur.

sample	size $x \times z$ (nm)	# atoms	# bilayers
long	1680×14.4	2 530 688	2
thick	420×57.6	2 531 536	8
small	420×14.4	632 884	2

TABLE I: Summary of the simulation details

The simulated systems consist of a layered Ni-Al nanofoil composed by a stacking of bilayers each made up of one slice of Ni and one slice of Al with and Ni-Al interfaces oriented normal to the [001] direction. One bilayer is $H = 7.2$ nm high and is formed by 16 atomic planes of Ni and 20 atomic planes of Al. The resulting stoichiometric ratio between Ni and Al is close to the equiatomic ($N_{\mathrm{Ni}}/N_{\mathrm{Al}} = 1.07$). To mimic the large number of alternated layers of metals, periodic boundary conditions were applied in the y and the z directions and free boundaries were set up along x.

As shown in Fig. 2 and Table I, three sizes of nanofoils were considered in this study: a small, a long and a thick sample. The small sample contains two bilayers and has a size of $420 \times 1.4 \times 14.4$ nm. This specific geometry is a reference system as it was used in our previous approaches focused on N2M [16, 19]. The long sample is 4 times as long and the thick sample 4 times as thick as the small one. The long sample was chosen to avoid any spurious effect related to a wide heat conduction zone. The thick sample was considered in order to study phase transformations and microstructure formation during the initial stages of the reactive wave propagation. In any case, an elongated geometry was chosen in order to allow for wave propagation.

The three atomic systems were created at 300 K, with the well-suited lattice parameters and the corresponding velocities. They were next relaxed at 300 K in isothermal-isobaric ensemble (NPT) using the Nose-Hoover thermostat and Parrinello-Rahman barostat over 0.4 ns. Afterward, a small section (i.e. 50 nm) on the left side of the samples was locally heated to induce the reaction. To realize that, the atoms in the section were integrated for 0.1 ns in the isothermal-isobaric ensemble (NPT) to reach the ignition temperature $T_{\mathrm{ig}} = 1200$ K, when all other atoms in the system were kept in the adiabatic-isobaric ensemble (NP$\mathcal{H}$). After the ignition, the thermostat was removed and system evolved within the NP$\mathcal{H}$. The thermostatting and barostatting time scales are 0.2 and 2.0 ps, respectively. The time-step is equal to 2 fs. This procedure allows to create the conditions close to experimental one, where the local heating produces the propagation of the reaction wave.

In order to follow the thermal and chemical evolutions, we divided the simulation box into cells

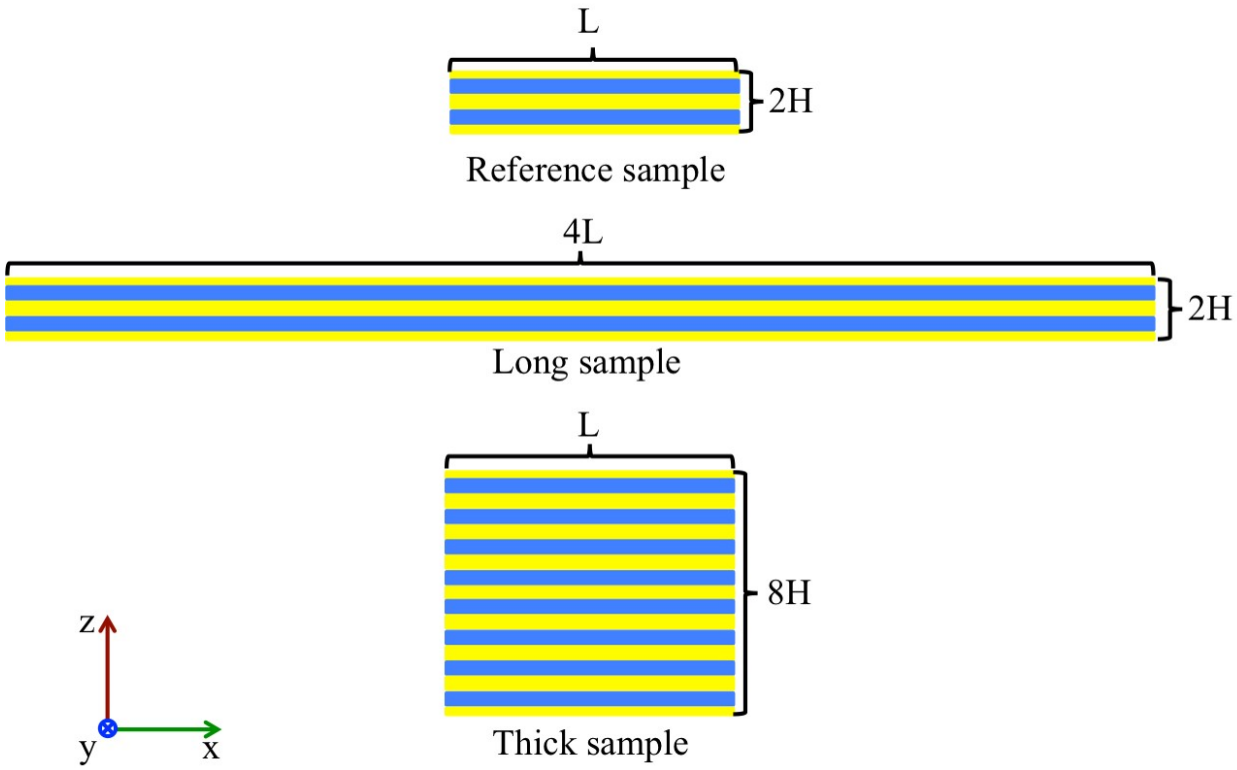

FIG. 2: Schematic representation of two samples used in the simulation. Yellow (light grey) is Ni and blue (black) is Al. Note that the proportions in x and z are not realistic. The thick sample is 7 times longer than it is thick.

of about 4 nm along the x direction where relevant quantities were measured. Firstly, the local temperature was obtained by averaging the kinetic energy of each atom in a specific cell. Secondly, the local atomic percentage (at%) of each species (Al or Ni), with or without specification of the local configuration (*bcc*, *fcc* or liquid), was computed. To do so, the atoms were tagged according to their local environment: *fcc* (refers to pure Ni and Al crystal), *bcc* ($B2$-NiAl intermetallic phase) and *liquid* (see [12] for more details).

III. RESULTS AND DISCUSSIONS

A. Reference sample

Figure 3 represents the temperature profiles along the sample at different times. After initiation, a thermal wave propagated across the foil without any heat supply. While the right part of the profile is smooth and dominated by conduction, the left part exhibits a complex shape which deforms over time. At later times ($t > 13$ ns), two flat regions (plateaus) were clearly identified at

two characteristic front temperatures T_c^{mix} and T_c. In order to understand the exothermic behavior of the propagation and the existence of two combustion temperatures, the elemental processes were investigated using the structure analysis.

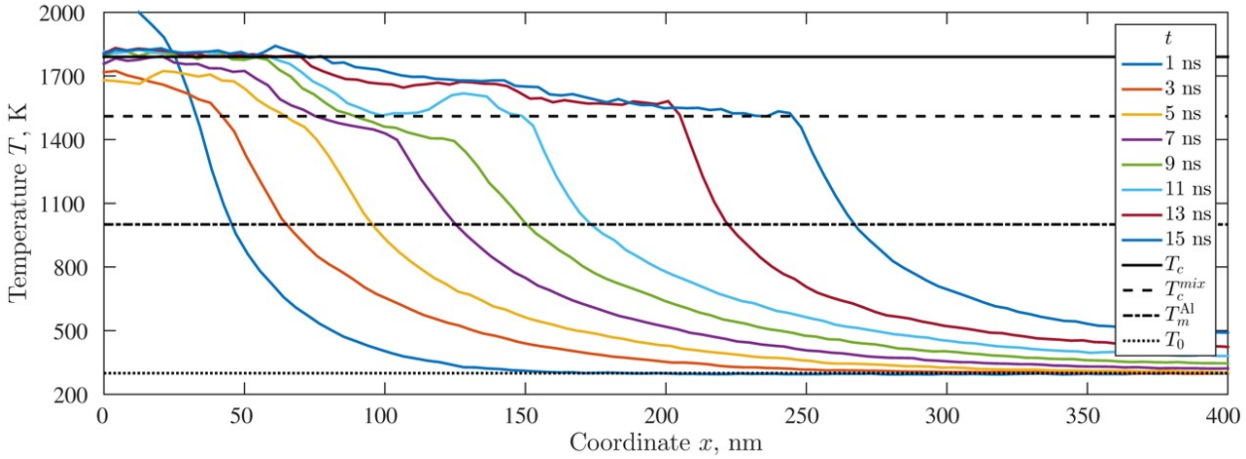

FIG. 3: Temperature profiles. The horizontal lines indicate the initial temperature, T_0, the melting temperature of Al, T_m^{Al}, the combustion temperatures, T_c^{mix} and T_c, corresponding to the first and the second plateau. The temperature profiles are plotted every 2 ns.

For example, the snapshot of the slice $0 < x < 100$ nm is shown in Fig. 4a-b at 3 ns. The corresponding temperature profile and mole fraction profiles of *bcc* Ni+Al, *fcc* Ni and *fcc* Al are represented in Fig. 4c. In the snapshots, several regions can be identified. On the left, the temperature is close to its maximum value and the two species form a liquid solution. On the right, where the temperature is below the melting temperature of Al, both metals remain solid (*fcc*-Al and *fcc*-Ni). In the middle (right part), solid nickel coexists with a liquid solution of Ni and Al. The stretched fingers of nickel embedded in a liquid alloy are typical of SHS propagation in N2M. In the left side of the middle, the presence of a region filled with $B2$-NiAl is noticed.

The most common way to characterize a front is to determine its velocity. The position of the front, defined by the position of the inflection point on the temperature profile (Fig. 3), was plotted as a function of time (blue circle in Fig. 4c). It is noteworthy that the dependence was linear and the speed constant. The thermal wave propagation was typical of a stationary combustion regime. Several other indicators can be chosen to follow the front propagation as shown in Fig. 4c:

- the Al melting front (green triangle);
- the Ni melting front (green diamond);

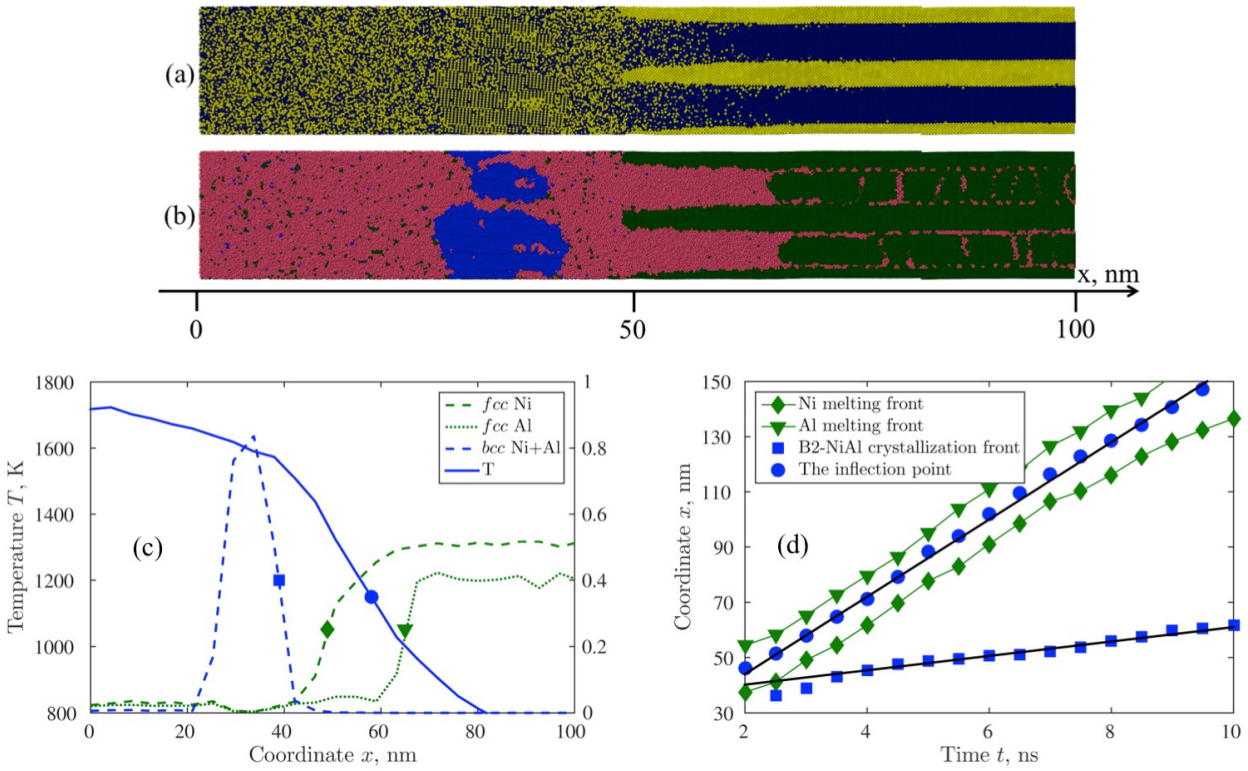

FIG. 4: Snapshots of the part of the sample with $0 < x < 100$ nm at 3 ns: (a) yellow is Ni and dark blue is Al; (b) after the modified Ackland analysis, red is liquid, blue is *bcc* and dark green is *fcc*. (c) Quantitative structure analysis combined with temperature profile. Points indicate the positions of different fronts. (d) Positions of the fronts over time. The front position is given by the inflection point of the corresponding profile (see (c)). For interpretation of the references to color in this figure legend, the reader is referred to the web version of this article.

- the $B2$-NiAl crystallization front in the direction of the reactive wave propagation (blue square);

Figure 4d shows the evolution over time of such points and allows for certain observations. First, the propagation of the front given by the inflection point on the temperature profile is controlled by dissolution, because it is always in between the melting fronts of Ni and Al (reactive dissolution zone). The front velocity as extracted from the slope of the linear fit gives the value of 14.2 m/s. Secondly, another reactive front follows the dissolution and is associated with the crystallization of $B2$-NiAl. The $B2$-NiAl crystallization velocity is much slower, with a value of 2.6 m/s. A typical temperature profile such as the one at 11 ns in Fig. 3, results from the superposition of 2 reactive fronts induced by two processes: the first front is produced by exothermic dissolution and mixing while the second front, which follows the first one, relates to the crystallization of $B2$-NiAl.

In the absence of heat loss, the heating of the right side of the sample was observed (see Fig. 3). That relates to the heat conduction from the high temperature (reacted) zone to the low temperature (unreacted) zone (see the zone with $300 < x < 400$ nm in Fig. 3). This type of behavior is typical of systems with a broad conduction zone, as wide as the length of the sample. The width of the region dominated by conduction is easily evaluated as $\Delta x = \kappa/v$, where the front velocity is $v = 14.2$ m/s and the thermal diffusivity at $T = 300$ K, $\kappa = 4.71\,10^{-6}$ m^{2}s^{-1} was obtained as in [19] in the case of an equiatomic system. This provides an estimation of the preheated zone $\Delta x(T_0 = 300\,\mathrm{K}) = 332$ nm, which corresponds to 79 % of the total length of the system. We also observed that the heating of the right side of the sample is responsible for the acceleration of the reactive front (for $t > 11$ ns). To avoid that inconvenience, a sample elongated along the x direction was considered for further investigation.

B. Long sample

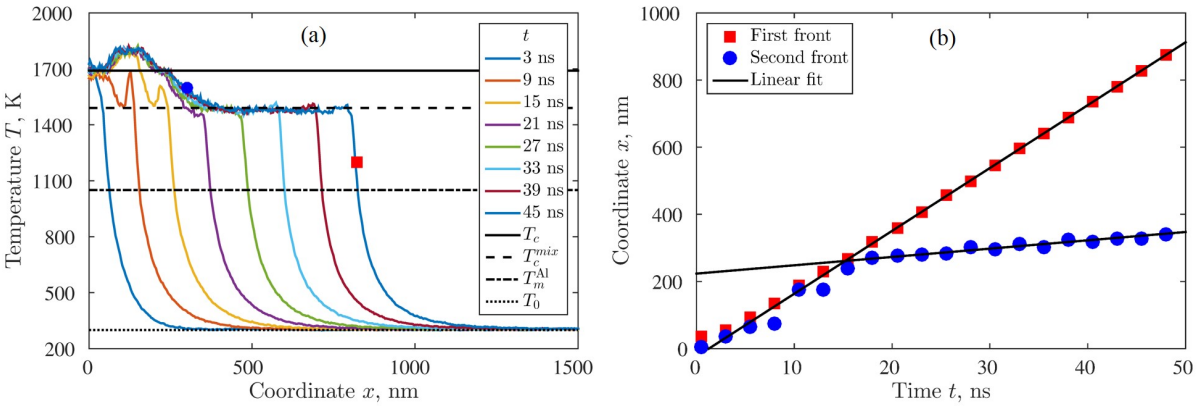

FIG. 5: (a) Temperature profiles along the front, at several times. The horizontal straight lines correspond to characteristic temperatures: the initial temperature T_0, the melting temperature of Al T_m^{Al}, the combustion temperature associated with the exothermic dissolution T_c^{mix} and the combustion temperature T_c. The temperature profiles are plotted every 6 ns. (b) Positions of the two reactive fronts as a function of time. Units: temperature in K; length in nm, time in ns.

Fig. 5a shows the evolution of the temperature profile in the system, along the x direction. After the thermalization stage ($t = 0.4$ ns), the whole system reached a temperature of 300 K. After the pulse of local heating ($T = 1200$ K for 0.1 ns), the temperature is transferred to adjacent regions by conduction. The initial step function was relaxed in a smooth curve while the ignited part began to react. The temperature increased to 1700 K (3 ns). The system was long enough

to avoid any global heating in the unperturbed zone (50 - 1680 nm). Careful examination of the temperature profiles revealed interesting features. At $t = 9$ ns, the profile was bimodal. Both humps have a maximum temperature of around $T = 1700$ K. At $t = 15$ ns, the left peak grew and expanded while the right one was smoothed. At $t = 21$ ns and at later times, the temperature profiles adopted a very specific shape: one hump that slowly changed into a smooth profile and a plateau. Both propagated along the sample without significant deformation. As for the small system, the MD simulations of the long system proved that the reactive wave is the superposition of two fronts. We speak of the "first" and "second" front in order to distinguish the two.

The position of the first front at $t = 45$ ns corresponds to the red square marker in Fig. 5a. The position of the second front was chosen by the position of the inflection point on the forehead peak, as shown in 5a by the blue bullet. The coordinate of the fronts over time is plotted in Fig. 5b. For the first front, the dependence was linear and the speed constant. The first front propagation was typical of a stationary combustion regime. The second front followed the first one, for about 15 ns. The average velocity was estimated at 16.4 m/s. The fronts then separated: the first one propagated at a much higher velocity of 18.7 m/s, while the second one moved more slowly at a constant velocity of 2.5 m/s. The velocity of the second front is of the order of magnitude of the crystallization velocity calculated using another simulation procedure (see B).

Figures 6 give an instantaneous image of the system in the very first stage of the propagation process, at $t = 8$ ns, before the appearance of the double-hump shape (see Fig. 5a - $t = 9$ ns). Snapshot 6a shows that different zones coexist in the reactive part of the sample:

1. The reacted zone on the left with the ordering of Ni and Al atoms.

2. The mixing zone corresponding to a liquid solution of Ni and Al.

3. The zigzagged region (pointed-shaped layers) associated with the progressive dissolution of Ni into Al liquid. The fingers consist of the remaining Ni solid reactant.

4. The unreacted Ni/Al multilayer in the solid state.

Snapshot 6b shows the same section of the system with atoms labeled as in the modified Ackland analysis [12]. Atoms in the *bcc* local configuration coexist with liquid atoms in zone (1). Zone (2) is filled with liquid atoms. The extended fingers of the region (3) correspond to *fcc*-Ni atoms. The unreacted zone (4) mainly contains *fcc* atoms. The thin red lines are associated with defects in the Al solid layers.

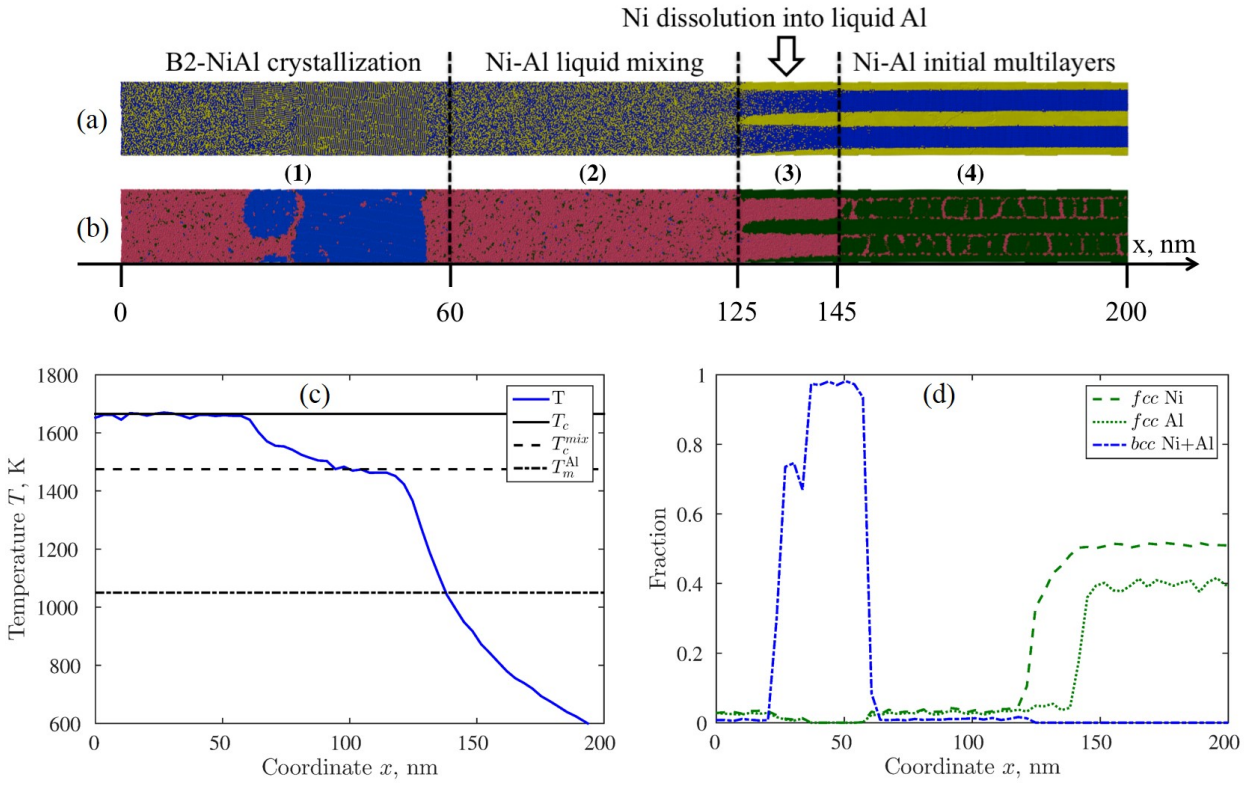

FIG. 6: Snapshots of a section of the sample $0 < x < 200$ nm at 8 ns: (a) with atoms labeled by their chemical identity (Al = dark blue, Ni = yellow); (b) with atoms labeled as in the modified Ackland analysis. Red is liquid, blue is *bcc* and dark green is *fcc*. (c) Temperature profile corresponding to this section. (d) Atomic% of Ni, Al in *fcc* local configuration and at% of Ni and Al in *bcc* local configuration along the section of the front (x, nm). For interpretation of the references to color in this figure legend, the reader is referred to the web version of this article.

The corresponding temperature profile along the front of the same zone is plotted in Fig. 6c. We note the existence of two plateaus associated with two characteristic temperatures: T_c and T_c^{mix}. From 0 to 50 nm, the temperature profile is flat. In the zone 50-90 nm, a smooth profile joins the two plateau temperatures. The second plateau is detected from 90 to 120 nm. For larger x-values, the temperature decreases slowly due to the heat transfer. The temperature profile can also be divided into 4 x-zones which precisely correspond to those detected in snapshots 6a and 6b. The temperature scale itself can also be divided as shown by the horizontal lines in Fig. 6c. Pure conduction is observed from the melting temperature of Al, T_m^{Al}, to the initial temperature. Temperatures in between T_m^{Al} and T_c^{mix} relate to the melting of Al, the progressive dissolution of Ni into liquid Al and the exothermic intermixing between the two metals. The temperature T_c^{mix} can thus be considered as the combustion temperature of mixing T_c^{mix}. The upper part of

the temperature profile, from T_c^{mix} to T_c is due to another exothermic process associated with the crystallization of a new phase A careful comparison with the local concentration profiles is also

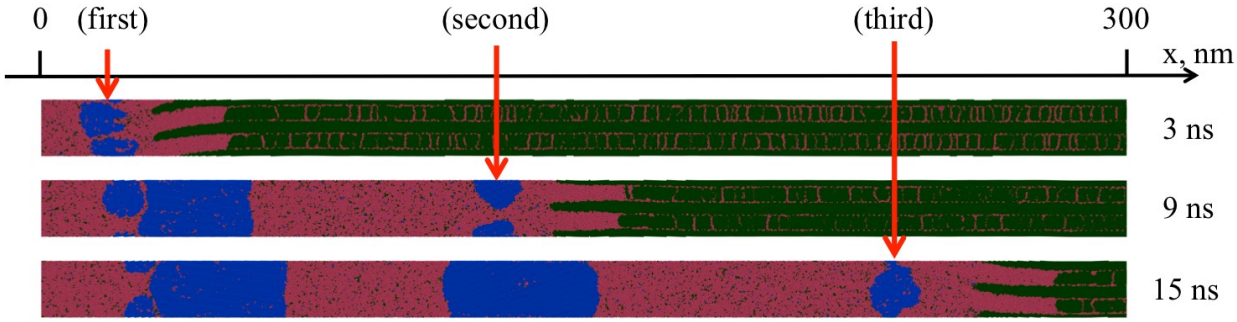

FIG. 7: Snapshots of the long sample with $0 < x < 300$ nm at 3, 9 and 15 ns. Red arrows indicate the positions of the high-temperature peaks in the corresponding temperature profiles in Fig. 5a. For interpretation of the references to color in this figure legend, the reader is referred to the web version of this article.

instructive. Atoms rearranged into a solid $B2$-phase occupy most of system from 10 to 60 nm. In the zigzag zone, *fcc*-Ni atoms are still present, whereas *fcc*-Al atoms are absent. In the non-reacted region, the fraction of *fcc*-Al atoms is slightly lower than that of *fcc*-Ni atoms because of all the defects detected in the Al layers.

A complex behavior of the crystallization front was observed during the first 17 ns (see Fig. 5a). The temperature profiles for times of less than 17 ns are characterized by two peaks at high temperature. Indeed, each time an NiAl nucleus appears, the temperature jumps to a higher value. Positions of the high-temperature peaks at 3, 9 and 15 ns correlate well with the positions of the newly-nucleated $B2$-NiAl grains. The snapshots of the system at the corresponding times are shown in Fig. 7. The positions of the peaks are indicated by the arrows. From 9 to 15 ns, the heat release due to the formation of the first and the second set of grains was relaxed. Thus, only one larger hump characterizes the left part of the profile even though it results from two successive nucleations. After 17 ns, no formation of new $B2$-NiAl grains was observed and the crystallization front moved in a steady-state regime, starting from the last-formed grain.

Combining the microstructure analysis and the temperature profile allowed us to detect the underlying reactive processes. After ignition, Al layers melt, solid Ni progressively dissolves into molten Al, Ni and Al atoms mix, heat is released and liquid solution Ni+Al is formed, in equiatomic ratio, at a temperature well below the melting temperature of the intermetallic NiAl. The Ni/Al liquid zone is thus in a metastable state that corresponds to the undercooled NiAl compound.

All conditions are required for the solidification of NiAl. This secondary process responsible for propagation thus relies on the exothermic formation of NiAl. Grain nucleation is very rapid, as fast as the dissolution rate.

C. Thick sample

The front propagation in the thick sample (see Fig. 2) exhibits the same characteristics as those observed in the long system. The main difference concerns the larger number of $B2$-NiAl grains which are formed during propagation.

The evolution (shape and size) of grains includes several stages, such as nucleation (Fig. 8a), growth (Fig. 8b-c) and coalescence (Fig. 8d-f). At 2 ns, nuclei appear at the edges of the solid fingers. Half a nanosecond later, the size of the existing grains has quickly enlarged while others have nucleated. At 3 ns, NiAl-grains and Ni-fingers are dissociated, due to the fast propagation of the dissolution front. Small grains disappear in favor of a big one. The grain morphology and texture of the crystallized region will be described in a subsequent section.

In what follows, we analyze the different stages of the microstructural evolution during the passage of the front through a slice $44 < x < 48$ nm into the sample where the grains are formed. To do so, several indicators were followed including the local temperature T, the fraction of atoms according to their chemical identity and to their local configuration (*bcc* or *fcc*).

The degree of mixing is also an important tool to study the homogeneity of the system. Here, a new mixing parameter M is introduced for an equiatomic Ni-Al system. It is based on the determination of a local mole fraction, n, for each atom in the system. The procedure for calculating n includes several steps. First, all the atoms inside a sphere with radius r around a reference atom are determined. Secondly, these atoms are separated according to their chemical species. In the case of the Ni-Al system, the mole fraction of Ni is determined as $n = N_{\mathrm{Ni}}/(N_{\mathrm{Ni}} + N_{\mathrm{Al}})$. The radius r must be large enough to include at least one neighbor shell for each phase existing in the system. The Ni-Al RDF functions of the different phases are shown in Fig. 9a. As can be seen, the optimal choice of the radius is $r = 0.3$ nm. This distance can be taken as a limit between short- and long-range orders, as it includes one neighbor shell of Ni, Al and liquid Ni-Al alloy, and two neighbor shells of the $B2$-NiAl. Examples of the spherical atomic clusters of radius 0.3 nm around a reference atom are given in Fig. 9b. Atoms are extracted from the cut of the long sample with $350 < x < 500\,\mathring{A}$ and with one half of the bilayer in the z direction ($0 < z < 35\mathring{A}$). The total number of the atoms in such clusters varies

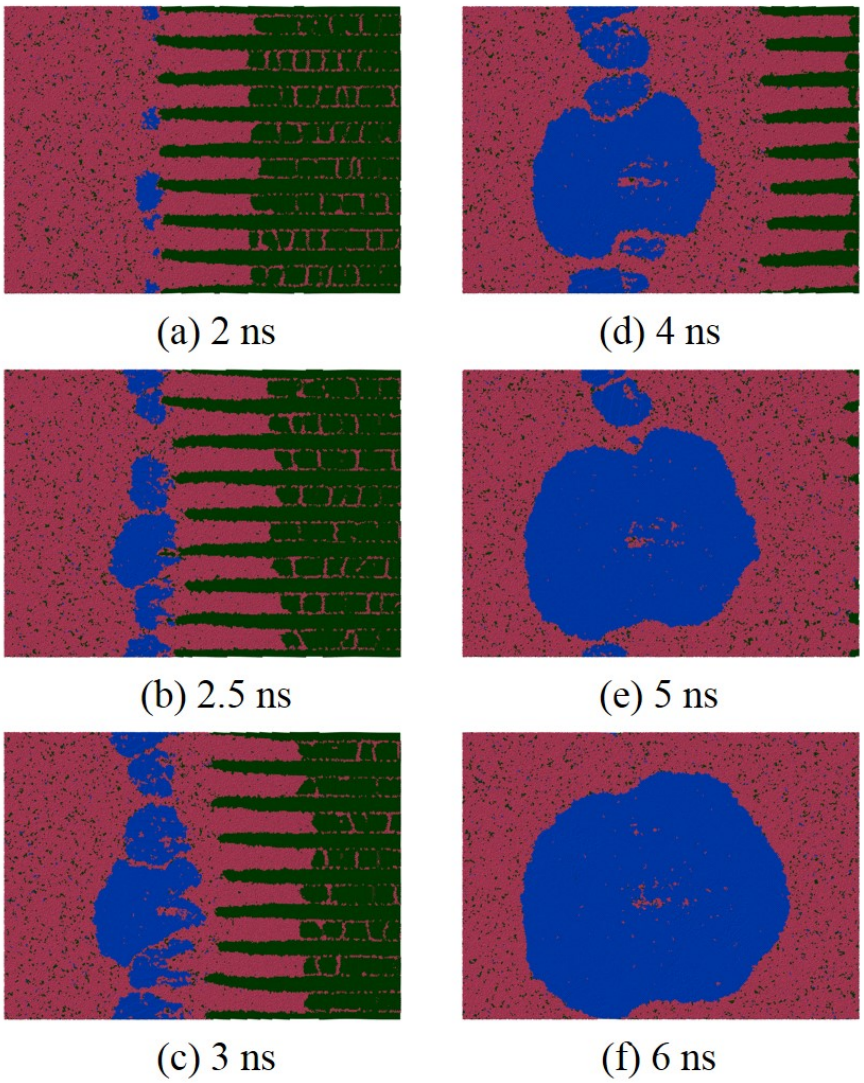

FIG. 8: Snapshots of a region of the thick sample with $20 < x < 100$ nm at several times. Atoms are labeled as in the modified Ackland analysis: red is liquid, blue is *bcc* and dark green is *fcc*. For interpretation of the references to color in this figure legend, the reader is referred to the web version of this article.

from 11 to 13, which is enough to calculate the local mole fraction n. As seen in Fig. 9b, the intermixing in the system can be locally characterized by n: for increased mixing of the Ni-Al layers, the value of the local mole fraction tends to $n = 0.5$ (in the case of equiatomic stoichiometry).

A quantitative analysis can be performed by defining the mixing parameter M as a "mesoscopic" quantity, which takes into account all the local mole fractions in a relatively small volume (less than the volume of the whole system but larger than 3 Å). The mixing parameter for a bilayered Ni-Al system (Al layer between two Ni layers) was defined by Xu et al. [11], who used a mole fraction

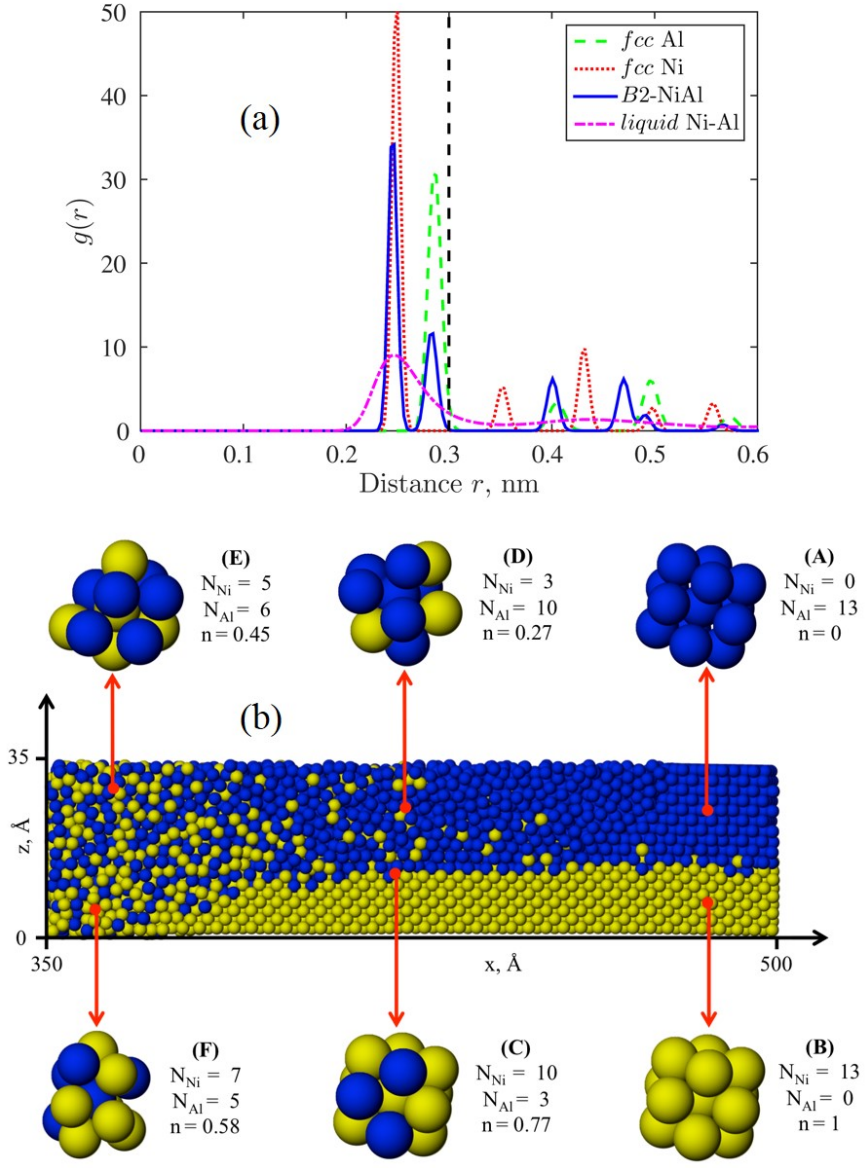

FIG. 9: (a) Radial distribution functions of the three solid phases in the Ni-Al system at 100 K and Ni-Al liquid at 2000 K. The vertical line indicates the distance from the reference atom, at which a minimum of at least one neighbor shell of each phase is included. (b) The multiphase sample in the middle represents the cut of the long sample with sizes of $350 < x < 500\mathring{A}$ and $0 < z < 35\mathring{A}$ at 1 ns. Atomic clusters with a radius of 0.3 nm around the reference atom are extracted from the different phases of the sample, e.g. (A) solid Al (*fcc*); (B) solid Ni (*fcc*); (C) Ni-rich solid solution; (D) Al-rich liquid alloy; (E) and (F) liquid Ni-Al alloy. N_{Ni} and N_{Al} are the numbers of Ni and Al atoms in the cluster, and $n = N_{\mathrm{Ni}}/(N_{\mathrm{Ni}} + N_{\mathrm{Al}})$ is the local mole fraction (mole fraction of Ni in the cluster).

of thin thin layer in the middle of the sample. Nevertheless, this definition is not applicable to systems with more than two bilayers. Here, the mixing parameter M is defined for an equiatomic

system with arbitrary geometry. In the 1D notation, the mixing parameter M for a single slice is defined as:

$$M = \frac{4 \cdot \sum_{\ell=1}^{N_{\text{slice}}} (n_\ell - 0.5)^2}{N_{\text{slice}}} \tag{1}$$

where N_{slice} is the number of atoms in the slice and n_ℓ is the local mole fraction of Ni in the sphere of 3 $\mathring{A}$ radius around ℓ-th atom. The same formula can be applied for mixing measurements of volumetric cells in 2D or in 3D. The mixing parameter M has two limits: $M = 0$ for homogeneous equiatomic alloy and $M = 1$ for totally separated unmixed layers of Ni and Al. As an example, the values of M for the heterogeneous system shown in Fig. 9b were computed in 1D and 2D cases. The 1D mixing parameter for slices of 10 nm width in the x direction is shown in Fig. 10a. In addition, the analysis for 2D cells (15 nm in the x direction and 3 nm in the z direction) is represented in Fig. 10b. Intermixed and unmixed regions are clearly separated. The mixing parameter M introduced here allows us to analyze the system both qualitatively and quantitatively. That makes M a useful tool for the study of the mixing process in a multiphase equiatomic system.

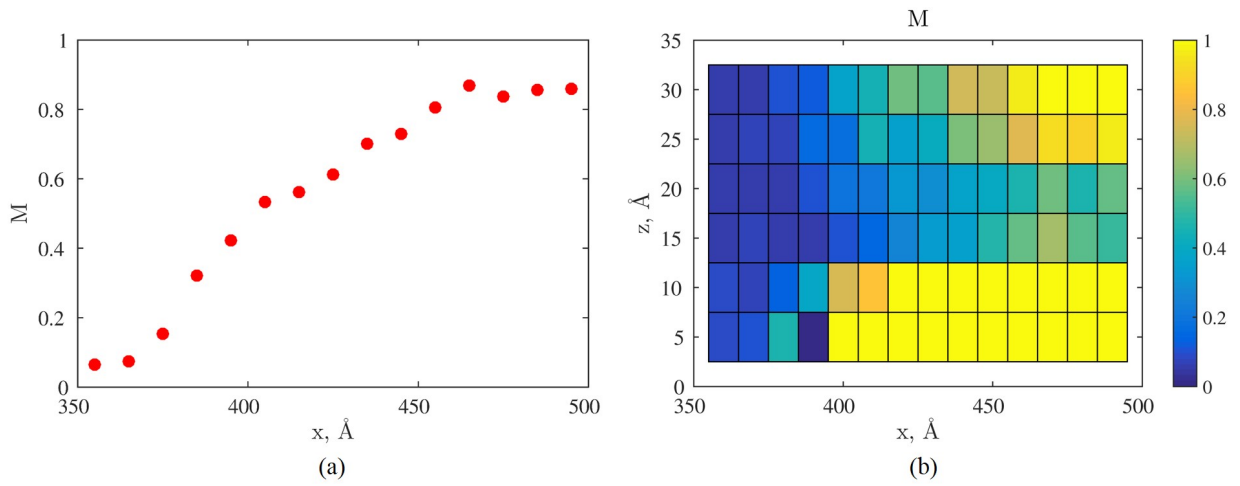

FIG. 10: The mixing parameter M analysis in (a) 1D and (b) 2D for the sample, which is shown in Fig 9b.

Figure 11a shows the evolution of the local quantities which are directly related to the structure and phase of the slice. Figures 11b and 11c show the thermogram (blue) and the enthalpy evolution (red). A comparative study of these results reveals several phenomena at work during the evolution. Six stages were identified for the slice in which the grains are formed:

I. The temperature increases due to the heating by conduction. The heat is transferred from adjacent cells. No transformation is noted.

II. The temperature increases up to a value larger than the melting temperature of Al. The fraction of *fcc*-Al decreases. This stage corresponds to the phase transformation

$$\mathrm{Al_{sol}} \rightarrow \mathrm{Al_{liq}}$$

III. During stage III, from $t = 1.1$ to 2.6 ns, the temperature increases from T_m^{Al} to 1300 K while the fraction of *fcc*-Ni starts to decrease slowly. The more pronounced variation in M indicates a significant mixing. This stage corresponds to the reactive dissolution of Ni into liquid Al at the interfaces.

$$\mathrm{Ni_{sol}} + \mathrm{Al_{liq}} \rightarrow \mathrm{Ni_{sol}} + (\mathrm{NiAl})_{\mathrm{liq}}$$

IV. The increase in temperature is less than that observed in stage III. But the change in microstructure is drastic. All *fcc*-Ni atoms disappear, together with a sharp variation in M. At the end of this period, mixing is complete.

V. The fraction of *bcc*-atoms increases together with temperature, and the enthalpy decreases further. All these indicators point to nucleation and the growth of a new phase $B2$-NiAl. The temperature during stage V remains below the melting temperature of the intermetallic compound NiAl. The equiatomic liquid solution $(\mathrm{NiAl})_{\mathrm{liq}}$ is therefore in a metastable state of the intermetallic compound. The undercooling of the slice occurs after the passage of the dissolution front. This situation is suitable for the rapid solidification of the new phase.

$$(\mathrm{NiAl})_{\mathrm{liq}} \rightarrow (\mathrm{NiAl})_{\mathrm{liq}} + \mathrm{NiAl_{sol}}$$

VI. For several nanoseconds during the last period, the increase in temperature and fraction of *bcc*-atoms is smooth as compared to stage V. Nevertheless, the enthalpy declines significantly. As shown in snapshots 8d-f, this behavior corresponds to the coalescence of the grains formed during stage V. During coalescence, the atoms surrounding the existing grains adopt a *bcc*-arrangement which is energetically more favorable. Atoms quit the disordered liquid solution to enlarge the $B2$-NiAl grains.

Three main exothermic processes were identified (see Fig. 11c):

- Dissolution and mixing, that produce $\Delta\mathcal{H}_{\mathrm{mix}} = 17$ kJ/mol of heat (59% of the total).
- The crystallization of $B2$-NiAl that produces $\Delta\mathcal{H}_{\mathrm{cr}} = 7$ kJ/mol of heat (24% of the total).

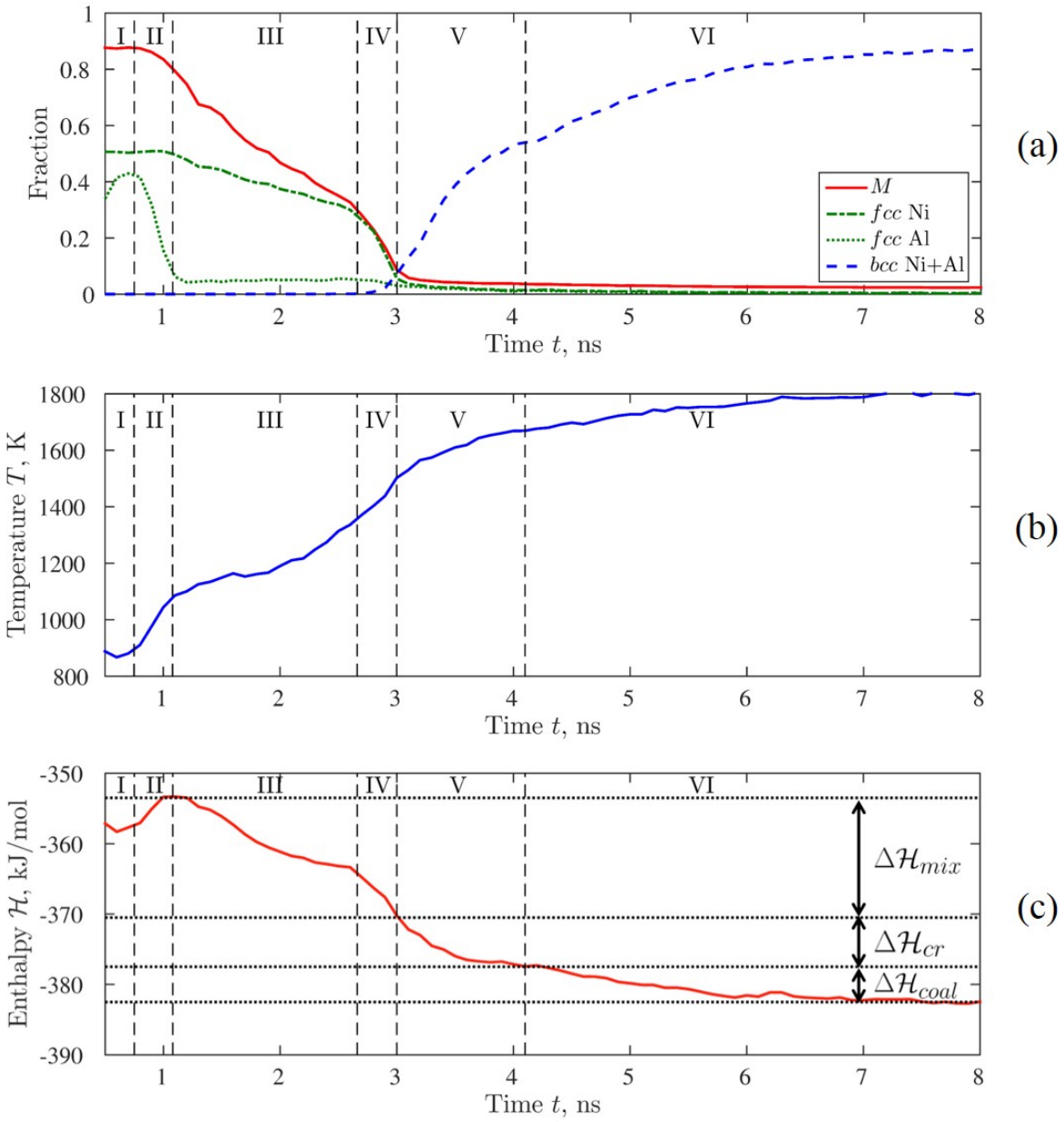

FIG. 11: (a) Structure analysis (b) Thermogram and (c) Enthalpy evolution in the slice $42 < x < 46.2$ nm of the thick sample. $\Delta\mathcal{H}_{\rm mix}$,$\Delta\mathcal{H}_{\rm cr}$,$\Delta\mathcal{H}_{\rm coal}$ are the heat released by mixing, $B2$-NiAl crystallization and coalescence of grains, respectively.

- The coalescence of grains, that produces $\Delta\mathcal{H}_{\rm coal} = 5$ kJ/mol of heat (17% of the total heat release).

During stage VI (4-8 ns), one grain grows at the expense of others as shown in Fig. 8d-e. If the grain is viewed as a sphere of diameter d, its size expands from $d_0 = 15$nm to $d_f = 60$nm. According to the literature, the grain boundary or interface energy, ϵ, of NiAl varies from 1.25 to

1.85 J/m^2 [24, 25]. The heat release due to the increase in grain size can be estimated as follows:

$$Q = \frac{6M_{\mathrm{mol}}\epsilon}{\rho}\left(\frac{1}{d_0} - \frac{1}{d_f}\right)$$

where $M_{\mathrm{mol}} = 0.0857$ kg/mol is the molecular mass and $\rho = 5860$ kg/m^3 is the density of NiAl. The rough estimation of the heat release due to grain growth is about 5.4 kJ/mol which corresponds to the value measured in MD simulations.

The same analysis can be carried out for the long sample presented in the previous section. The results are presented in Fig. 12. The heat release due to the different processes are: $\Delta\mathcal{H}_{\mathrm{mix}}$= 19 kJ/mol (56 %), $\Delta\mathcal{H}_{cr}$= 15 kJ/mol (44 %). In the case of a 2-bilayer system, only two grains were formed, as shown in Fig. 6a. After grain growth, the final stage VI is associated with the motion of the grain boundary out of the slice of reference. At 6 ns, only one grain remains in the slice while the second grain has moved to the next slice, due to local fluctuations. This explains the constant enthalpy observed at the end of stage VI.

D. Influence of the initial premixing

In order to investigate the effect of an initial premixing, a new procedure was applied to the small sample. It was first created at 100 K with the well suited lattice parameter and heated to 600 K with a temperature ramp of 2.5 K/ps. Then, it was thermalized (annealed) at 600 K over 6.4 ns and cooled to 300 K with a temperature ramp of 1.5 K/ps. After this specific annealing, the sample was locally heated to induce the reaction as presented in section II. The initial and annealed states of the system are shown in Fig. 13a. As can be seen in Figs. 13b-c, the annealing process induces the mutual diffusion and intermixing of Ni and Al atoms at the interfaces, with the formation of the premixed layers. The mixing parameter M shows that the mixing is quite limited in the initial sample.

The behavior was analyzed along the lines explained in section III A using the structure analysis together with the profile of indicators. Figure 14d shows the evolution over time of the position of the two fronts. The front velocity of the first front as extracted from the slope of the linear fit gives the value of 12.3 m/s. The $B2$-NiAl crystallization velocity is much slower, with a value of 3.8 m/s. These values for the small sample after 6.4 ns of annealing can be compared with the corresponding front velocities of the same sample without annealing. This allows us to determine the effect of annealing on the reactive wave propagation in the multilayered equiatomic Ni-Al system. The observed results is that the annealing process induces a decrease in the reactive dissolution (first)

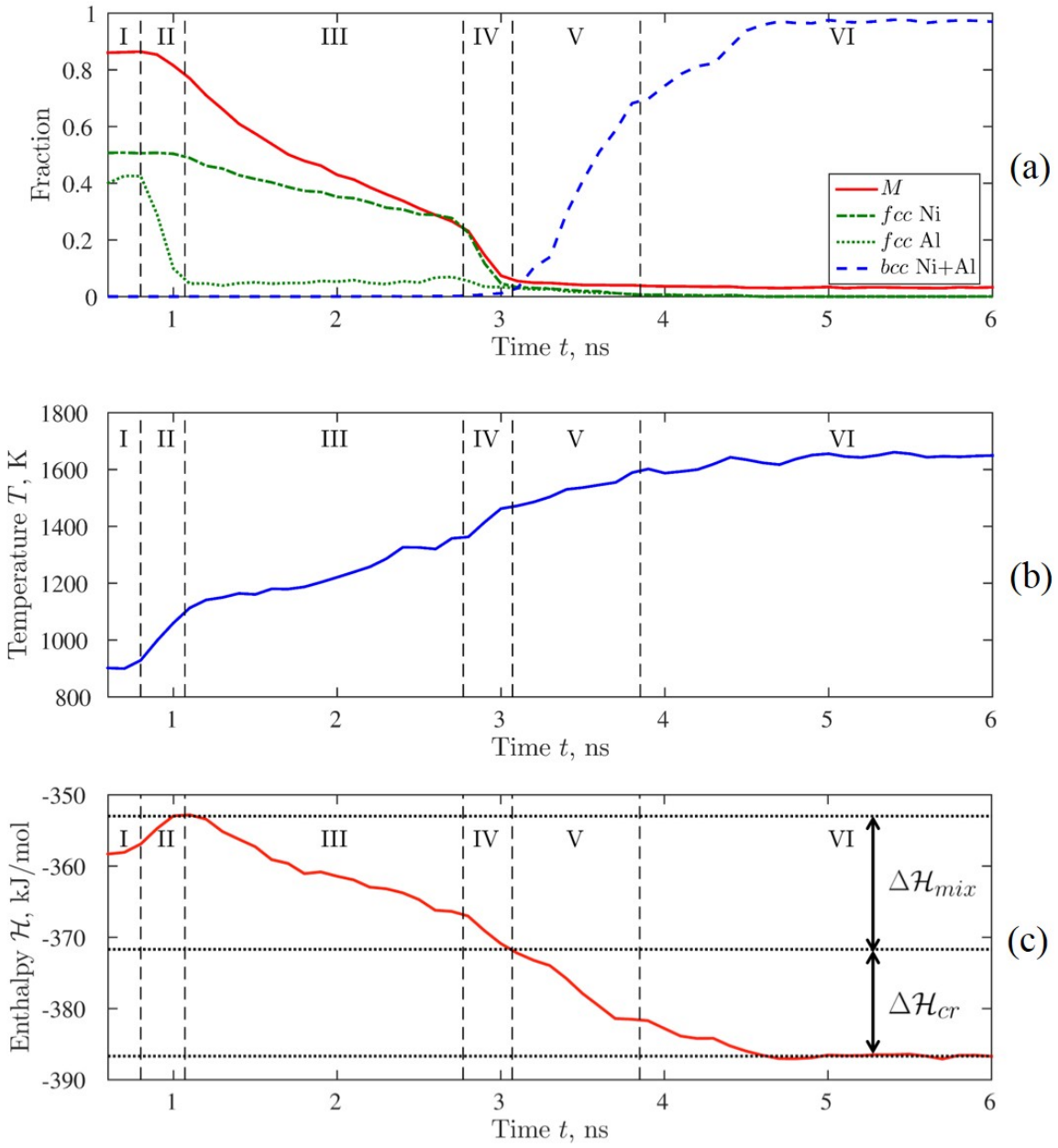

FIG. 12: (a) Structure analysis (b) Thermogram and (c) Enthalpy evolution in the slab $43.7 < x < 47$ nm of the long sample. $\Delta\mathcal{H}_{\text{mix}}$,$\Delta\mathcal{H}_{\text{cr}}$,$\Delta\mathcal{H}_{\text{coal}}$ are the heat released by mixing, $B2$-NiAl crystallization and coalescence of grains, respectively.

front velocity from the 14.2 m/s to 12.3m/s and an increase in the explosive crystallization (second) front velocity from 2.6 m/s to 3.8 m/s.

In addition, the annealing induces a slight effect on the microstructure formation, namely an increase in the number of $B2$-NiAl nuclei. Three successive nucleations were observed at the initial stages of the reactive wave propagation instead of two as in the long sample. The number of nuclei

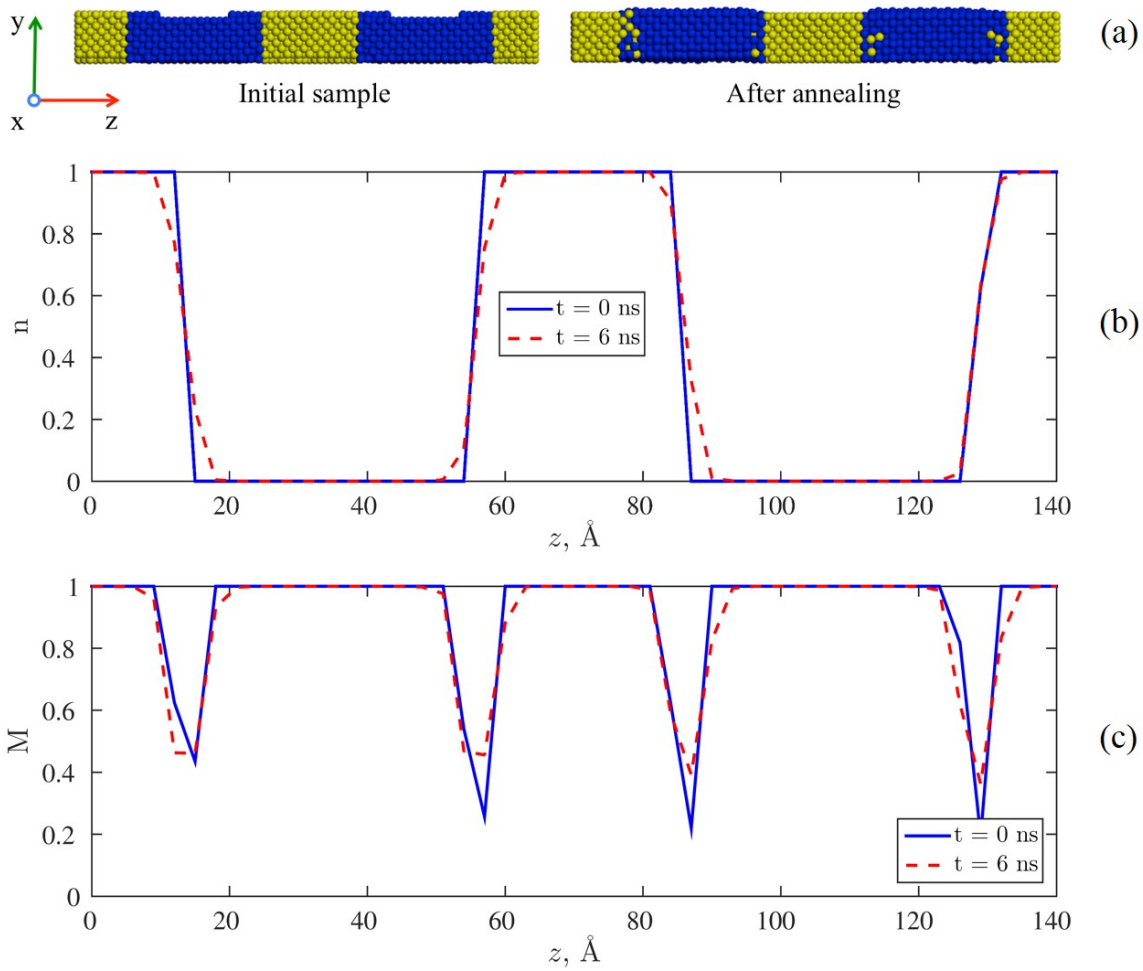

FIG. 13: (a) Snapshots (yz-view) of the small sample before (left) and after (right) annealing for 6.4 ns at 600 K. The defect observed in the left-hand figure is an artefact due to periodic boundary conditions. Initial and final states were analyzed by means of the profiles of (b) the mole fraction of Ni n and (c) the mixing parameter M in the z direction.

per bilayer is 0.75 for the thick sample, 1 for the long sample without annealing and 1.5 for the small sample with annealing.

Finally, the energetic characteristics of the phase transformations during the reactive wave propagation were estimated. It was found that the dissolution and mixing processes produced 18 kJ/mol (55% of the total), the $B2$-NiAl explosive crystallization produced 11 kJ/mol of heat (33% of the total) and the coalescence of grains produced 4 kJ/mol of heat (12% of the total heat release). These values correlate well with the corresponding values for the long sample.

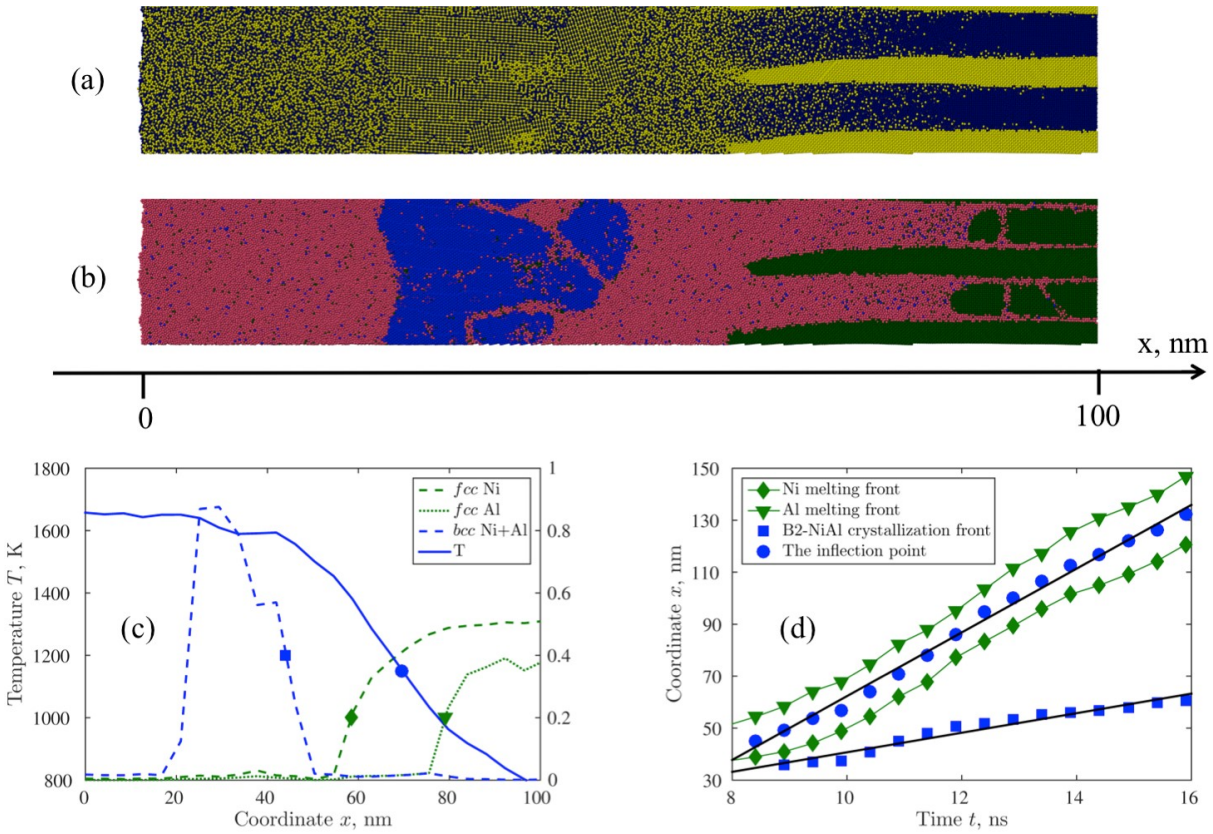

FIG. 14: Snapshots of the part of the sample with $0 < x < 100$ nm at 10.8 ns: (a) yellow is Ni and dark blue is Al; (b) after the modified Ackland analysis, red is liquid, blue is *bcc* and dark green is *fcc*. (c) Quantitative structure analysis combined with temperature profile. Points indicate the positions of different fronts. (d) Positions of the fronts over time. For interpretation of the references to color in this figure legend, the reader is referred to the web version of this article.

E. Microstructure analysis

The nuclei appear at the edge of the Ni solid fingers as shown in Fig. 8. It would be interesting to characterize the grains. Do they all present the same orientation? How does the orientation of the grains evolve during crystallization?

A texture analysis was developed to characterize the structure of the grains formed during the crystallization of $B2$-NiAl. Let us consider the system at $t = 2.5$ ns in which several NiAl-grains have been formed (see Fig. 8b). For each *bcc*-atom ℓ-atom, the neighboring atoms j-atom of the same species were identified within a sphere of 3.5 Å. The histogram of their relative distances, from the reference atom, is plotted in Fig. 15a. Most of the nearest neighbors are located around the value of the lattice parameter $a_{\mathrm{NiAl}} = 2.86$ Å, the expected value in a perfect NiAl-crystal. A small number of neighboring atoms are closer to the reference atom. The second peak corresponds

to Ni(Al)-atoms that arrive in substitution of Al(Ni)-atoms: $\sqrt{3}a_0/2 = 2.58\mathring{A}$ (Fig. 9a).

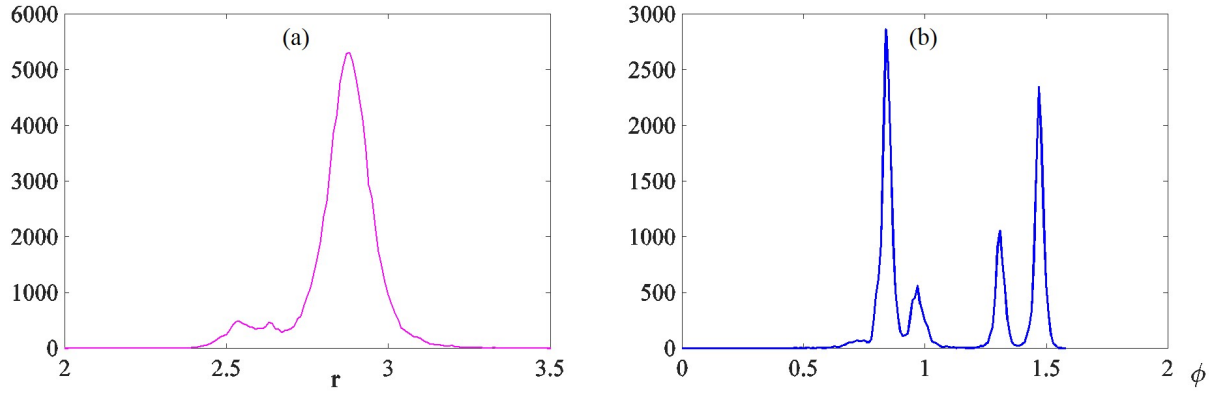

FIG. 15: (a) Histogram of the relative distances between each *bcc*-atom and its nearest neighbors of the same species, within a sphere of 3.5 Å, at 2.5 ns. (b) Histogram of the larger elevation angle $|\phi_3|$, in absolute value (expressed in radians). The angle ϕ_3 is between one of the 3 directions drawn between each *bcc*-atom and its nearest neighbors of the same species, when the number of nearest neighbors is larger than 4.

As soon as the nearest neighbor atoms are identified, the spherical coordinates of each vector $\overrightarrow{\ell j}$ can be calculated. The local orientation was determined by the largest elevation angle ϕ_3, in absolute value (see A). Only reference-atoms with a number of nearest neighbors larger than 4 were considered. As shown in Fig.15b, four spatial orientations were observed. If we consider only atoms with 6 nearest neighbors (nn), a smaller number of atoms will be concerned and labelled by the local orientation. The condition of 6 nn is equivalent to rejecting all atoms located in the shell of the grain and atoms surrounded by a defect. Indeed, Fig. 17a shows 3 orientations selected during grain formation from 2 to 5 ns.

Figure 16 gives a snapshot of the system, in the region where grains were formed. The grains are colored according to their the local orientation. The corresponding atomic configuration is plotted for the three observed orientations:

- Grain A (green grain) is characterized by an orientation $(100)[0\bar{1}1]$. The atoms in the plane $(0\bar{1}1)$ are represented in Fig. 21b. Another grain, with the same orientation, formed in the upper side of the zone.

- Grain B (red grain) shows a slight difference in orientation $\vec{e_3} \sim \vec{1_z}$ in the z-direction ($\phi_3 = 1.44$) and is rotated about the z-axis by $\pi/4$. The orientation matrix reads: $g = (hkl)[uvw] \sim (\bar{1}\bar{1}0)[001]$. Another red grain formed below the green grain A.

- Grain C (magenta) contains atoms in the bottom and in the upper part of the sample because of periodic boundary conditions. Its orientation slightly differs from that of grain B, $\phi_3 = 1.30$, and $g = (hkl)[uvw] \sim (\bar{1}\bar{1}0)[001]$.

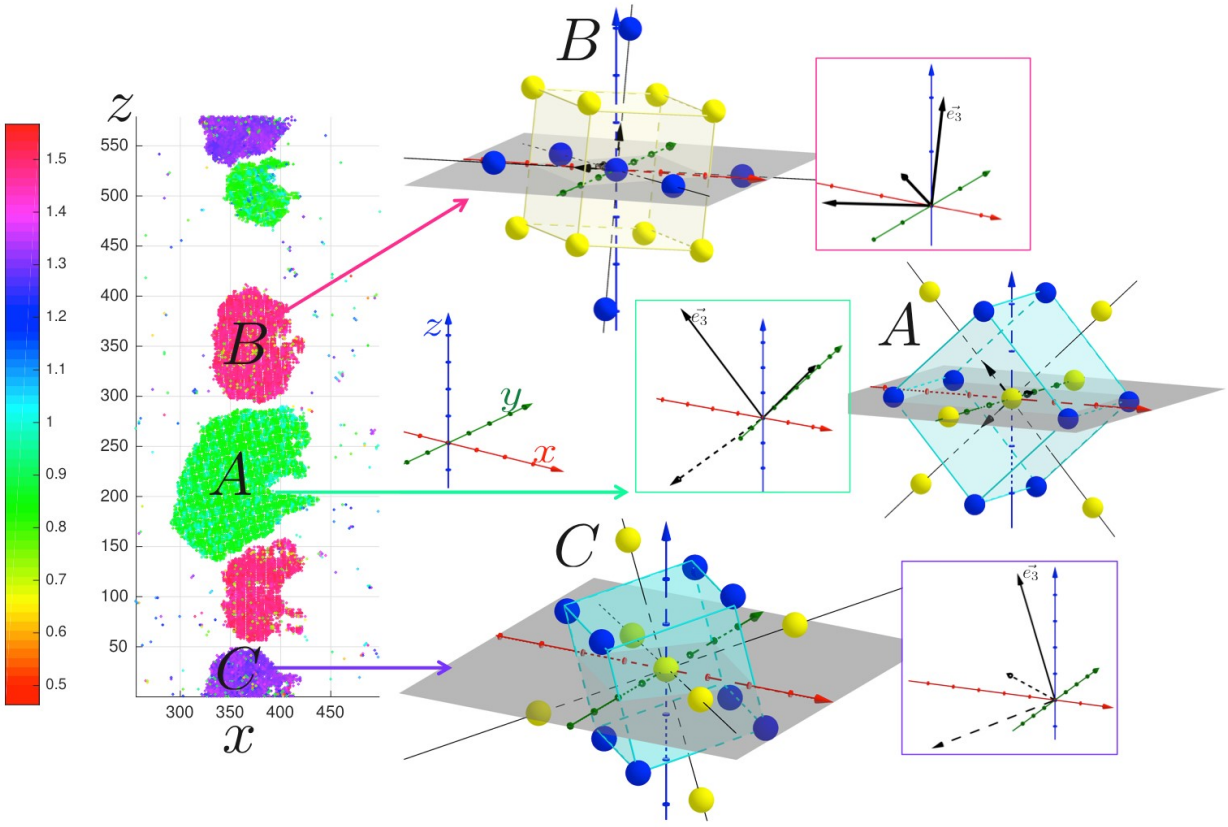

FIG. 16: Orientation of the grains. NiAl *bcc*-atoms are colored according to the value of ϕ_3 (see text), at $t = 2.5$ ns.

The evolution of the texture of the grains is depicted in Fig.17. Just after the nucleation of the grains, at $t = 2$ ns, two then three peaks characterize the distribution of the angle ϕ_3. During the growth of the grains, it is obvious that the green grain becomes larger at the expense of the red and magenta ones. The peaks close to $\phi_3 = \pi/2$ dwindle and, finally, disappear at $t = 5$ ns. The orientation of isolated grains are subject to small fluctuations. For instance, we note a slight shift $(2-3°)$ of the peak around 1.4, from $t = 3$ to 4 ns. The same is noted for the dominant peak which shows a refocusing around the final value $\phi_3 = 0.83$. This happens when $B2$-NiAl grains detach from the Ni fingers. As shown in the plot of the cumulative function of the density of orientation (Fig. 17b), the growth of the green grain is much faster than those of the red and magenta ones. After 4 ns, the green grain continues to swell due to the absorption of the contiguous smaller grains

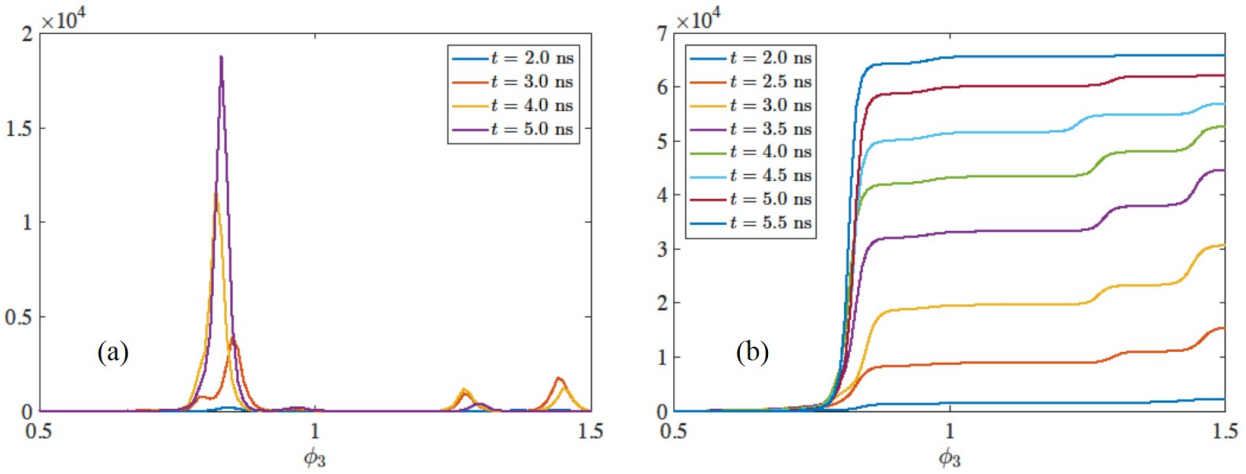

FIG. 17: (a) Histogram of the local orientation ϕ_3 (elevation angle of $\vec{e_3}$) of the *bcc*-atom, with its 6 nearest neighbours, belonging to crystallized grains. (b) Cumulative function of the previous function.

and precipitation from the liquid phase. To understand the mechanisms of nucleation and growth during the crystallization process, we focus on the behavior of one grain. The evolution of the

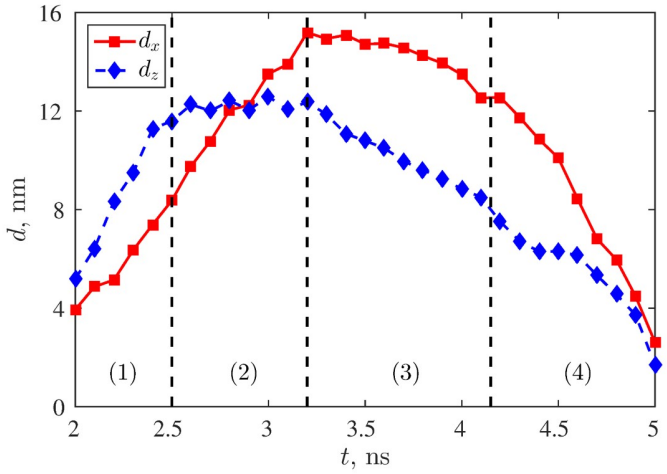

FIG. 18: Evolution of the size of a grain in the x and z directions. The vertical dashed lines indicate the 4 stages identified during the complete process.

red grain B is represented in Fig. 18, where d_x and d_z are the sizes of the grain in the x and z directions, respectively. The first stage (see Fig. 18(1)) is characterized by a linear (constant rate) growth. The grain is limited at the right side by the solid Ni layer. This is the reason why the grain growth rate is higher in the z direction (15.2 m/s), than in the x direction (9.4 m/s). In the second stage (see Fig. 18(2)), the grain continues to grow in the x direction at the same rate, but has stopped growing in the z direction, because of the presence of the other grains in this direction.

During this stage, grain boundaries form perpendicular to the z direction between the red grain B and the contiguous green grains. At the third stage (see Fig. 18(3)), the size of the grain starts to decrease in both the x and z directions. Two processes are responsible for this:

- the rearrangement of the atoms at the grain boundaries due to the orientation of the neighboring grains (absorption of the red grain by its larger neighbors) in the z direction;

- dissolution of the atoms from the interface into the liquid Ni-Al alloy in the x direction.

As seen in the figure, these two processes are not equivalent: the absorption of the grain is much faster (4.9 m/s) than the dissolution (2.1 m/s). During the fourth stage(see Fig. 18(4)), the decrease in grain size accelerates in both directions. Finally, the grain disappears between 5 and 5.1 ns.

F. Sustainability of the grains formation

The $B2$-NiAl grains result from an heterogeneous nucleation at the Ni tips just behind the dissolution front (see, for example, Fig. 8a). Only three successive nucleations were observed in the direction of the reactive wave propagation in the long sample (see Fig. 7). We here propose an explanation for that lack of sustainability. Let us focus on a layer just behind the moving dissolution front. The corresponding local temperature and local mole fraction of *bcc*-atoms are plotted in Fig. 19a and 19b.

Because of the fast intermixing, the liquid layer just behind the dissolution zone became homogeneous at the same time as melting of Ni happened (see the limit between the stages IV and V in Figs. 11 and 12). This is a good situation with a 50/50 composition to form the intermetallic compound. No variability of the local composition was observed. The behavior of the local temperature is more puzzling. As shown in Fig. 19a, the temperature is not constant. The temperature results of the balance between four processes:

- heat release due to the reactive dissolution;

- heat conduction from the reactive dissolution zone to the unreacted zone;

- heat release due to the crystallization of $B2$-NiAl;

- heat conduction from the $B2$-NiAl grains to the liquid zone.

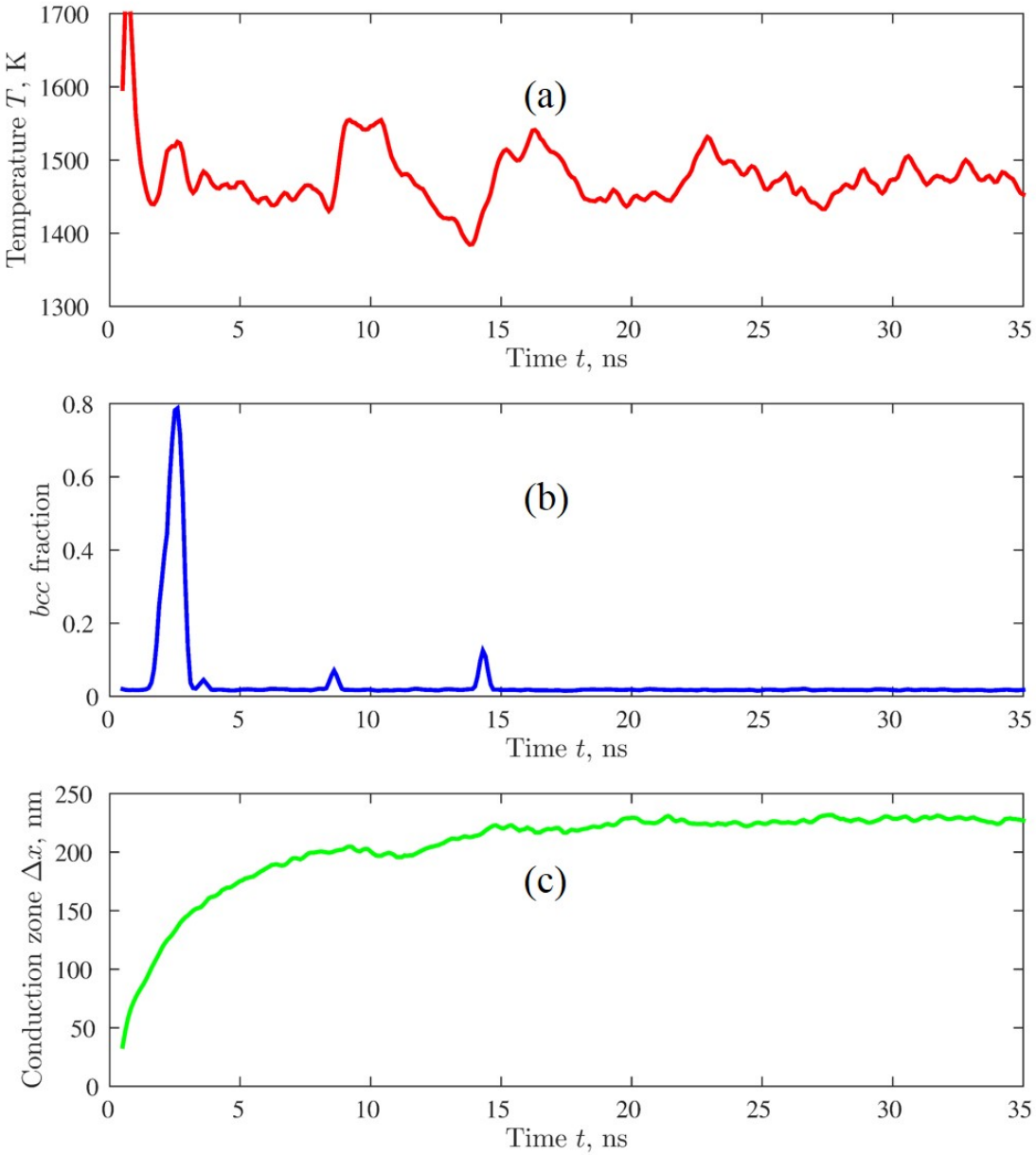

FIG. 19: (a) Temperature and (b) *bcc* mole fraction in a small region just behind the reactive dissolution front vs time. (c) Time dependence of the conduction width. The conduction zone is evaluated as the width of region with a temperature in between 400 K and 1050 K.

Initially, the ignition process is realized by a local heating of the left side of the sample. The initial temperature profile looks like a step function. The large temperature gradient induces a large heat flux to the unreacted region. Meanwhile the heat release by the crystallization of $B2$-NiAl compensates the heat transfer. (Fig. 19 from 0 to 5 ns). After the grain formation, the reactive dissolution moved faster than the grain growth in the x direction (lack of *bcc* formation around 5 ns in Fig. 19b). Then, the temperature decreases due to conduction toward the unreacted zone

rather than it increases due to conduction from the crystallized grain. The slight decrease of the temperature was followed by the B2-NiAl nucleation. The same behavior was observed from 10 to 15 ns. After 15 ns, a competition between the heat fluxes was observed without further nucleation of new $B2$-NiAl grains. After 25 ns, the reactive dissolution front was so far from the last formed B2 grain that the two fronts were moving without reciprocal influence. For the dissolution-driven steady-state propagation, the heat release by dissolution is in equilibrium with the heat flux due to conduction toward the unreacted zone. In that case, the thickness of the conduction zone reaches its asymptotic value, defined as $\Delta x = \kappa/v$, as observed after 25 ns (see Fig. 19c) . The temperature of the liquid layer just behind the reactive dissolution zone also became constant close to 1500 K.

A decrease in temperature of the liquid layer behind the dissolution region was observed before any nucleation. That allows us to assume the local temperature is a main factor in the heterogeneous nucleation of the $B2$-NiAl grains from the Ni tips. The heterogeneous nucleation of B2-NiAl solid in Ni + Al equimolar liquid solution is favoured by the existence of Ni solid tips whereas the growth of the B2-NiAl phase is governed by the solid/liquid transformation. The second front lags continuously in comparison to the fast moving self-sustained dissolution front. To obtain a sustained reactive wave propagation with formation of $B2$ grains it is necessary to reduce the temperature just behind the reactive dissolution zone by initial premixing or heat losses.

IV. CONCLUSIONS

MD simulations are a powerful tool to observe the different phase transformations involved in the reactive wave propagation occurring in N2M. The analysis of simulations allows us to draw the following conclusions :

- A rapid solidification from the melt can be observed if the initial temperature is low enough.
- In that case, the reactive wave consists of two stages. The first stage can propagate independent of the second one.
- The velocity of propagation in the reactive wave is principally determined by the velocity of propagation of the first stage.
- The first stage results from a dissolution/mixing process.
- Two combustion temperatures are associated with the reactive wave.

- The products of the reactive wave are likely nano-grains of NiAl, separated by a liquid phase of Ni + Al.

- Post-combustion processes are typical of a two stage combustion front. They are associated with the NiAl grain growth and coalescence of grains.

- The combustion wave is assumed to be sequential. The processes involve different exothermic transformations associated with heat of reaction. A quantitative value is estimated by MD simulations.

A specific tool dedicated to texture analysis of the product was also developed and used in the characterization of NiAl intermetallic grains. More generally, this tool can be used to map the crystallographic orientations of the phase formed during MD simulations.

Acknowledgments

The use of computational facilities at the Computing Center of the University of Bourgogne, PSIUN-CCUB, is gratefully acknowledged.

Appendix A: Texture analysis tool

We here develop a new analysis tool to describe microstructure. Our aim was to determine the structure of the polycrystalline $B2$-NiAl phase observed in the simulations. The structure is given by the position and the orientation of the grains with respect to the sample, as shown in Fig. 20. The orientation is referred to as the *texture* and is given by the orientation coordinates.

In a perfect $B2$-NiAl solid phase, each atom ℓ - the so-called reference atom - is surrounded by a first shell of 6 atoms of the same species (either Ni or Al, depending on the species of the reference atom). These six neighboring atoms $j\,(j = 1, 6)$ are aligned, two by two, along three directions (d_1, d_2, d_3). Each vector $\overrightarrow{\ell j}$ is specified by its spherical coordinates (r_j, θ_j, ϕ_j). The vector $\overrightarrow{\ell j}$ with the largest elevation angle ϕ_j is chosen as the direction d_3 associated with the reference atom ℓ. The unit vector $\vec{e_3}$ is along d_3. The two other vectors $\{\vec{e_1}, \vec{e_2}\}$ are located in the plane perpendicular to $\vec{e_3}$. The vector $\overrightarrow{\ell j}$ with the highest elevation angle ϕ_j, in absolute value, and a positive azimuth, $\theta_j > 0$, is chosen as the direction d_1 associated with the reference atom ℓ, with $\vec{e_1}$ as the unit vector. The unit vector $\vec{e_2}$ is chosen along the remaining direction d_2. It is such that $\vec{e_1} \otimes \vec{e_2} = \vec{e_3}$. This simple method allows us to define a local referential $\{\vec{e_1}, \vec{e_2}, \vec{e_3}\}$ associated with each atom

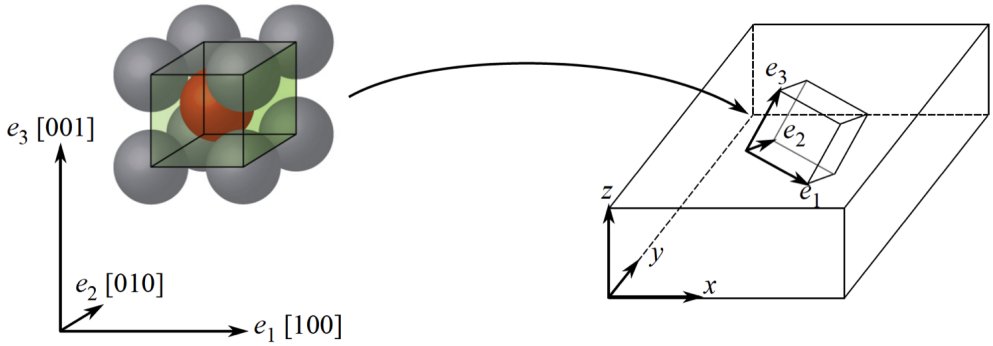

FIG. 20: Schematic representation of a crystallite embedded in a large system. The referential $\{\vec{e_1}, \vec{e_2}, \vec{e_3}\}$ corresponds to the referential of the crystallite.

in a local $B2$-NiAl configuration. This procedure is easily implemented. As an example, Fig. 21 shows the local environment of the Al-atom, a, in the crystallized $B2$-NiAl grain. The first six Al-neighbors of a are aligned along three directions. The vector $\vec{e_3}$ points in the direction with the larger elevation angle. The four other atoms lie in a plane perpendicular to $\vec{e_3}$, as expected in a $B2$-NiAl.

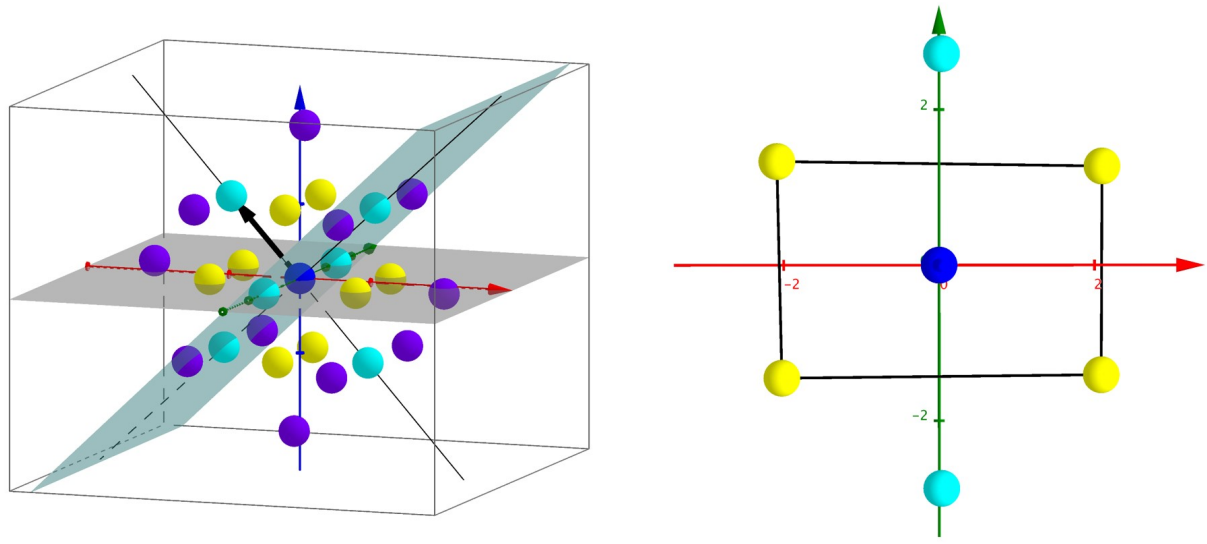

(a) (b)

FIG. 21: (a) The reference atom and its neighboring atoms. The reference atom is an Al atom, in blue. Al-atoms in the first shell are light blue and Ni atoms are yellow $r < 3.5$Å. Al-atoms in the second shell are violet $3.5 < r < 4.5$ Å. The box corresponds to the orientation of the sample. (b) Corresponding $(0\bar{1}1)$ plane with the closest nearest neighbors of the reference atom.

Having specified the sample coordinate system and the crystal coordinate system associated

with a grain, an orientation is then defined as the position of the crystal coordinate system with respect to the specimen coordinate system (for a detailed description see [27]). That is

$$K_{\text{grain}} = g\, K_{\text{sample}} \tag{A1}$$

where $K_{\text{grain}} = \{\vec{e_1}, \vec{e_2}, \vec{e_3}\}$ and $K_{\text{sample}}\{\vec{1_x}, \vec{1_y}, \vec{1_z}\}$ are the crystal and sample coordinate systems, respectively, and g is the orientation matrix, which embodies the rotation of the sample coordinates onto the crystal (grain) coordinates. The orientation matrix, g, is a square matrix of nine elements:

$$g = \begin{pmatrix} \cos\alpha_1 & \cos\beta_1 & \cos\gamma_1 \\ \cos\alpha_2 & \cos\beta_2 & \cos\gamma_2 \\ \cos\alpha_3 & \cos\beta_3 & \cos\gamma_3 \end{pmatrix} \tag{A2}$$

The first row is given by the cosines of the angles α_1, β_1, γ_1 between the first crystal axis, $\vec{e_1} = [100]$, and each of the sample axes, $\{x, y, z\}$. Similarly, the second and third rows are given by the cosines of the angles between the second crystal axis, $\vec{e_2} = [010]$, and the third one, $\vec{e_3} = [001]$, and the sample axis. The relation between the angle γ_3 and the elevation of $\vec{e_3}$ reads: $\gamma_3 = \pi/2 - \phi_3$. Another way to express g is in terms of the Miller indices:

$$g = (hkl)[uvw] \tag{A3}$$

The nine elements are non-independent variables since the vectors $\{\vec{e_1}, \vec{e_2}, \vec{e_3}\}$ are orthonormalized. For example, in the case of Fig. 21, the orientation matrix reads

$$g \approx \begin{pmatrix} 0 & 1 & 0 \\ -1 & 0 & -1 \\ -1 & 0 & 1 \end{pmatrix}$$

and $[hkl] = [0\bar{1}1]$ (see Fig.21b).

Appendix B: Crystallization velocity

The crystallization velocity of B2-NiAl was computed with a two-phase method very similar to the one used by Kerrache [26]. Three orientations of the solid-liquid interface were considered in the x direction: (100),(110) and (111). Each sample was created at a given temperature T in the range of 1200 - 1750 K with the corresponding lattice parameters and velocities (note that the melting temperature is 1780 K for this system). Typical sizes of the system are indicated in Table

II. Periodic boundary conditions were imposed in all directions. The runs were performed in the NPT ensemble. The initial sample was equilibrated over 0.2 ns. Then, one half of the sample with $0 < x < L_x/2$ was melted at 3000 K over 0.2 ns. A two phase system was obtained as shown in Fig. 22a. After that initial procedure to create the two-phase system, the system was evolved at a given temperature T over 2 ns.

orientation	size $x \times z$ (nm)	Q, kJ/mol	K, m/s
(100)	$86.9 \times 2.9 \times 2.9$	34	1091
(110)	$122.9 \times 2.9 \times 4.1$	18.8	252
(111)	$150.5 \times 4.1 \times 5.7$	15.2	172

TABLE II: Summary of the simulation details and parameters evaluated in MD simulations.

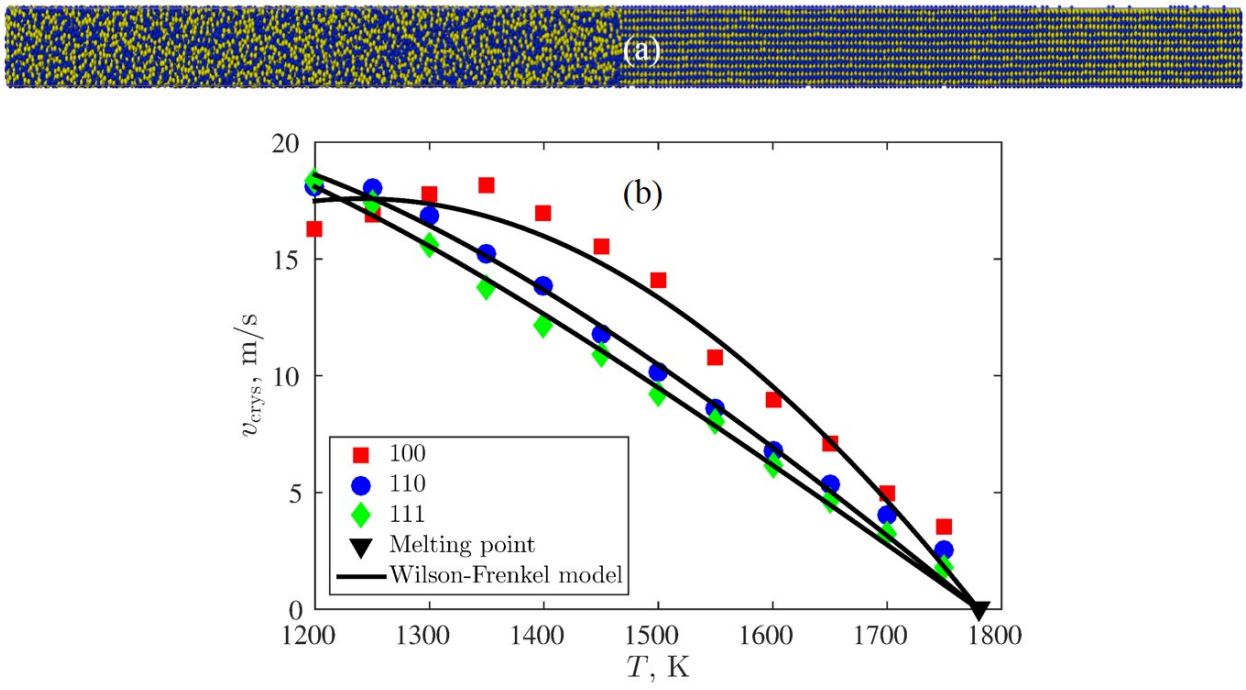

FIG. 22: (a) xz view of the two-phase sample with (100) orientation of the interface. (b) crystallization velocity v_{crys} as a function of temperature for the different orientations. More details are indicated in the text.

Two moving interfaces were observed due to the periodic boundary conditions. The length of the crystalline region was followed on time and the average crystallization velocity was estimated. The temperature dependence was approximated using the Wilson-Frenkel model [26] given by the

following expression:

$$v_{\text{crys}} = K \cdot \frac{T_m - T}{T} \exp\left(-\frac{Q}{k_B T}\right)$$

where v_{crys} is crystallization velocity, $T_m = 1780$ K is the melting temperature of B2-NiAl for the given EAM potential [22], Q is the activation enthalpy, k_B is the Boltzmann constant and K is a constant. The parameters estimated in MD simulations are listed in Table II for different orientations of the interface solid/liquid. Fig. 22 represents the crystallization velocity as a function of temperature for three orientations of the interface.

---

[1] T.W. Barbee and T. Weihs, U.S. Patent 5538795, July 23 (1996).

[2] T.P. Weihs, *Handbook of Thin Film Process Technology*, D. A. Glocker and S. I. Shah Eds., IOP Publishing, Bristol (1998).

[3] A.B. Mann, A.J. Gavens, M.E. Reiss, D. Van Heerden, G. Bao, T.P. Weihs, J Appl Phys. 82, 1178 (1997).

[4] J. Wang, E. Besnoin, A. Duckham, S. J. Spey, M. E. Reiss, O. M. Knio and T. P. Weihs, J. Appl. Phys. **95**, 248 (2004).

[5] A.S. Rogachev and A.S. Mukasyan, Comb. Expl. Shock Waves 46, 243 (2010).

[6] A.S. Rogachev, S.G. Vadchenko, A.S. Mukasyan, Appl. Phys. Lett. 101, 063119 (2012).

[7] I.E. Gunduz, S. Onel, C.C. Dourmanidis, C. Rebholz, S.F. Son, J. Appl. Phys 117, 214904 (2015).

[8] A.S. Rogachev, S.G. Vadchenko, F. Baras, O. Politano, S. Rouvimov, N.V. Sachkova, M.D. Grapes, T.P. Weihs, A.S. Mukasyan, Combustion and Flame. 166, 158 (2016).

[9] F. Baras, O. Politano, Phys. Rev. B. 84, 024113 (2011).

[10] J.C. Crone, J. Knap, P.W. Chung, B.M. Rice, Appl. Phys. Lett. 98, 141910 (2011).

[11] R.-G. Xu, M. Falk, T.P. Weihs, J. Appl. Phys. 114, 163511 (2013).

[12] V. Turlo, O. Politano, F. Baras, Acta Mater. 99, 363 (2015).

[13] N.S. Weingarten, W.D. Mattson, A.D. Yau, T.P. Weihs, B.M. Rice, J. Appl. Phys 107, 093517 (2010) .

[14] O. Politano, F. Baras, A.S. Mukasyan, S.G. Vadchenko, A.S. Rogachev, Surf. Coat. Technol. 215, 485 (2013).

[15] S. Zhao, T.C. Germann, A. Strachan, J. Chem. Phys 125, 164707 (2006).

[16] O. Politano, F. Baras, J. Alloy Compd 652, 25 (2015).

[17] M.J. Cherukara, T.P. Weihs, A. Strachan, Acta Mater 96, 1 (2015).

[18] A.S. Rogachev, S.G. Vadchenko, F. Baras, O. Politano, S. Rouvimov, N.V. Sachkova, et al., Acta Mater. 66, 86 (2014).

[19] V. Turlo, O. Politano, F. Baras, Acta Mater. 120, 189 (2016).

[20] A.S. Rogachev, Russ. Chem. Rev. 77, 21 (2008).

[21] see http://lammps.sandia.gov/; S. Plimpton, Journal Comp. Phys. 117, 1 (1995).

[22] G. Purja Pun, Y. Mishin, Phil. Mag. 8, 3245 (2009).

[23] G.J. Ackland, A.P. Jones, Phys. Rev. B. 73, 054104 (2006).

[24] Y. Amouyal, E. Rabkin, Y. Mishin, Acta Mater. 53, 3795 (2005).

[25] A.V. Evteev, E.V. Levchenko, I.V. Belova, G.E. Murch, Phys. Met. Metallography 113, 1202 (2012).

[26] A. Kerrache, J. Horbach and K. Binder, Europhys. Lett. 81, 58001 (2008).

[27] O. Engler, V. Randle, Introduction to Texture Analysis: Macrotexture, Microtexture, and Orientation Mapping, Second Edition, CRC Press. (2009).